Electronic Supplementary Material (ESI) for Energy & Environmental Science.

Supplementary Materials for

Modulating Multi-Hole Reaction Pathways for Photoelectrochemical Water Oxidation on Gold Nanocatalysts

Yuchao Zhang,[1§] Yunlu Zhang,[1] Wenxiao Guo,[1] Aaron C. Johnston-Peck,[2] Yue Hu,[1] Xuening Song,[1] and Wei David Wei*[1]

[1] Department of Chemistry and Center for Catalysis, University of Florida, Gainesville, FL 32611, United States

[2] Center for Functional Nanomaterials, Brookhaven National Laboratory, Upton, NY 11973, United States

Correspondence to: wei@chem.ufl.edu.

This PDF file includes:
Experimental section
Supplementary Notes 1 to 11
Figure S1 to S45
Table S1 to S5
References (1 – 26)

Experimental section

Materials: Tetrachloroauric acid ($HAuCl_4$, 99.99%), Titanium (IV) butoxide (97%), 1,2-Dihydroxybenzene (≥99%), 4-Nitrocatechol (97%), 3,4-Dihydroxybenzonitrile (97%), Sodium sulfite (≥98%), Methanol (99.8%), Ethanol (>99.5%), and Hydrochloric acid (HCl, 37%) were purchased from Sigma Aldrich. Sodium hydroxide (NaOH, >97.0%) was purchased from Fisher Scientific. Deuterated water (D_2O, 99.9%) were purchased from Cambridge Isotope Laboratories, Inc. All chemicals were used as received without further purification.

Instrumentation: Ultraviolet-visible (UV-vis) spectra were collected on a Shimadzu UV-2600 spectrophotometer. Scanning electron microscopy (SEM) images were collected on an FEI Nova Nano 430 SEM operated at 15 kV at the Nanoscale Research Facility of University of Florida (UF). Photoelectrochemical (PEC) measurements were controlled by a potentiostat (PGSTAT302N autolab, Metrohm). Additional dual mode bipotentiostat (BA) module and PX1000 module were used for dual-working electrode (DWE) PEC experiments. Three mono-wavelength LED lamps (470 nm, 530 nm, and 630 nm) controlled by PGSTAT302N were used as light sources. X-ray photoelectron spectroscopy (XPS) data were obtained using a PHI VersaProbe Scanning XPS Microscope (Al Kα) with an energy resolution of 0.1 eV. 0.21 kV Argon ions were used to neutralize surface charge. Adventitious carbon with the binding energy of 284.8 eV was used as a reference for calibration. Annular dark-field scanning transmission electron microscopy (ADF-STEM) imaging was conducted on a Cs-corrected Hitachi HD-2700C microscope equipped with a Cold-FEG and operated at 200 kV (located at BNL, Upton, NY). Images were acquired using a probe convergence angle of 23 mrad, with the inner collection angle of ADF detector at 53 mrad. Liquid chromatography-mass spectroscopy (LC-MS) data were obtained using an LCQ DECA quadrupole ion trap mass spectrometer with electrospray ionization (ESI) operating with

XCALIBUR 2.0.7. SP1. High-performance liquid chromatography (HPLC) was conducted using Agilent (Palo Alto, CA) 1100 series system consisting of G1313A autosampler, G1322A degasser, and G1312A binary pump. Mobile phase A was H_2O + 0.2% acetic acid and phase B was methanol + 0.2% acetic acid.

Fabrication of Au/TiO_2 electrodes: Rutile TiO_2 nanowire electrodes were fabricated using a hydrothermal method.[1] FTO substrates were first cleaned in a mixed solution of 10 mL of acetone, 10 mL of 2-propanol, and 10 mL of nanopure water for 1 h ultrasonication. FTO substrates then were rinsed using nanopure water, airdried, and placed at an angle against the sidewall of a 40 mL Teflon-lined autoclave. In a separate 100 mL beaker, 15 mL of nanopure water and 15 mL of concentrated HCl (37 wt%) were mixed, followed by addition of 500 μL of Ti (IV) butoxide. The solution was stirred for 5 min and poured into a 40 mL Teflon-lined autoclave containing FTO substrates. Hydrothermal synthesis was conducted in an oven at 150 °C for 5 h. Photochemical growth of Au nanoparticles (NPs) on TiO_2 electrodes was performed in a solution containing 200 μL of methanol, 250 μL of 10 mM $HAuCl_4$, and 4.8 mL of nanopure water in a 50-mL beaker. The solution was irradiated for 5 min with a 500 W Hg lamp (full spectrum). Briefly ultrasonicating electrodes in water (~ 5 s) removed Au NPs not strongly bound to TiO_2 nanowires. Electrodes were further annealed under 200°C for 10 min in a tube furnace. For fabricating DWE, a 10 nm Au film was deposited on Au/TiO_2 electrodes by sputtering (model KJL CMS-18 MULTI-SOURCE).

Fabrication of Au NP electrodes: A 10 nm Au film was deposited on FTO substrates by sputtering (model KJL CMS-18 MULTI-SOURCE). Further annealing under 600°C for 1 h converted the Au film to Au NPs.

Photoelectrodeposition of catechol and charging of modified electrodes: As-prepared Au/TiO_2 electrodes and Au NP electrodes were immersed in a 0.1 M catechol solution for 24 h in the dark and then an anodic bias of 1.0 V_{RHE} was applied to electrodes for 240 – 600 s under the irradiation of a 470 nm LED. After being modified with catechol, electrodes were rinsed with nanopure water to remove catechol weakly bound to the electrodes. Then electrodes were put into an unbuffered solution with pH 7.0 (0.1 M $NaClO_4$). A bias of 1.2 V_{RHE} was held for 1 h under 470 nm illumination to fully charge electrodes with hot holes. Those as-prepared electrodes were moved to a clean unbuffered solution with pH 7.0 for PEC water-oxidation measurement.

Photodeposition of catechol on Au/TiO_2 electrodes: As-prepared Au/TiO_2 electrodes were immersed in a 0.1 M catechol solution under the irradiation of a 470 nm LED for 10 h. After being modified with catechol, electrodes were rinsed with nanopure water to remove catechol weakly bound to the electrodes.

PEC measurement: Conventional PEC experiments were performed in a three-electrode electrochemical cell and DWE PEC experiments were performed in a four-electrode electrochemical cell, both with Pt as the counter electrode and Ag/AgCl as the reference electrode. For electrochemical impedance spectroscopy (EIS), experimental data were fitted and simulated using Nova 1.11 from Metrohm Inc. pH values of electrolyte solutions were measured using a pH meter, and pD values were calculated using the equation $pD = pH_{read} + 0.4$.[2] Concentrations of dissolved O_2 were measured using a YSI Professional Optical Dissolved Oxygen Meter. N_2 was purged into electrolyte for 1 h to remove dissolved O_2. It is noted that unbuffered solutions with pH 7.0 (0.1 M $NaClO_4$) and pH 13.6 (1 M NaOH) were used as electrolytes for main results in the manuscript. Buffer (e.g., PO_4^{3-}) was not used since previous works reported that buffer species influenced charge separations and surface proton transfer processes on semiconductors.[2-3]

Experimental results obtained in the buffered solution (0.1 M PO_4^{3-}) were only shown in the supplementary information for reference. It also needs to be noted that catechol molecules adsorb on Au via hydroxyl groups. When performing the reaction in alkaline solutions, the competitive adsorption between hydroxyl groups and OH^- ions in the electrolyte would further decrease the stability of Au/catechol electrodes for water oxidation. Therefore, all those catechol-modified electrodes were tested in the neutral medium.

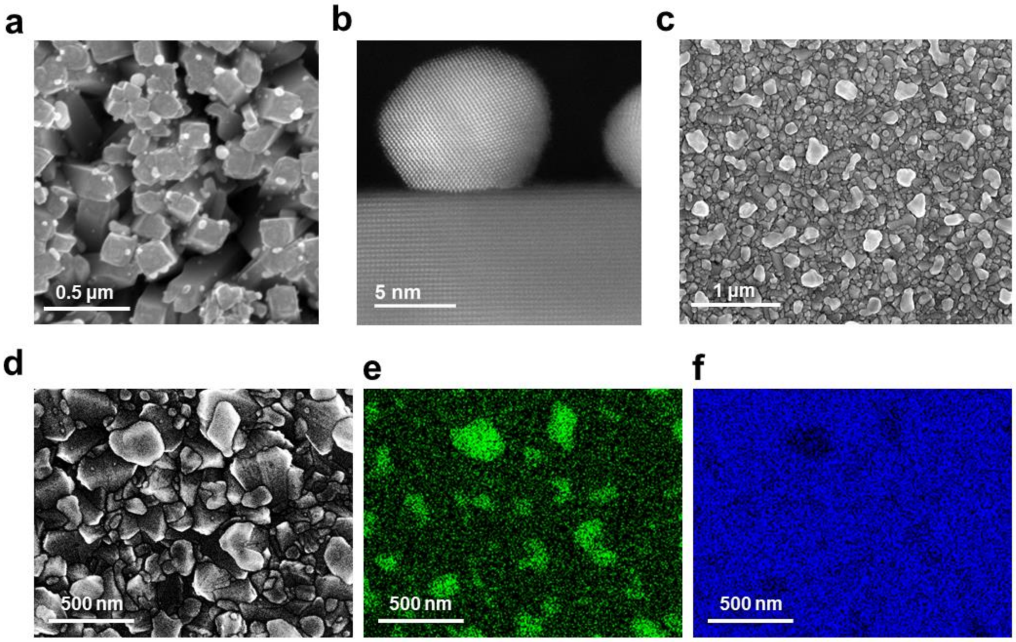

Figure S1. Morphologies of Au/TiO_2 and Au NP electrodes. (**a**) SEM image of Au/TiO_2 heterostructures. (**b**) ADF-STEM image showing an intimate physical contact between Au and TiO_2, which ensured an efficient charge transfer across Au/TiO_2 interfaces. (**c**) and **(d)** SEM images of a Au NP electrode. (**e**) EDS mapping of Au on the same area of (**d**). (**f**) EDS mapping of Sn on the same area of (**d**). EDS mapping was used to reveal sizes and distributions of Au NPs on FTO.

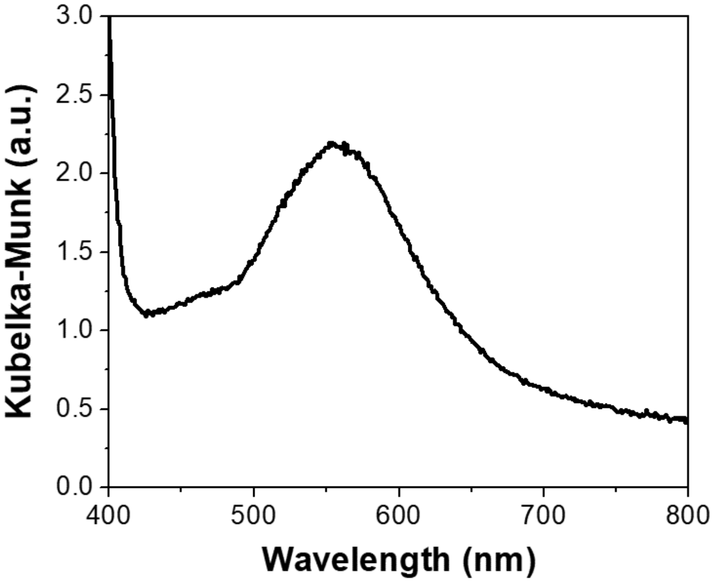

Figure S2. UV-Vis spectrum of a Au/TiO$_2$ electrode. FTO glass was used as reference. The major visible-light absorption peak located at 550 nm with a weaker absorption around 460 nm. In this work, to photo-excite Au/TiO$_2$, three mono-wavelength LED lamps (470 nm, 530 nm, and 630 nm) were used as light sources with light intensities adjusted to 500 mW/cm^2.

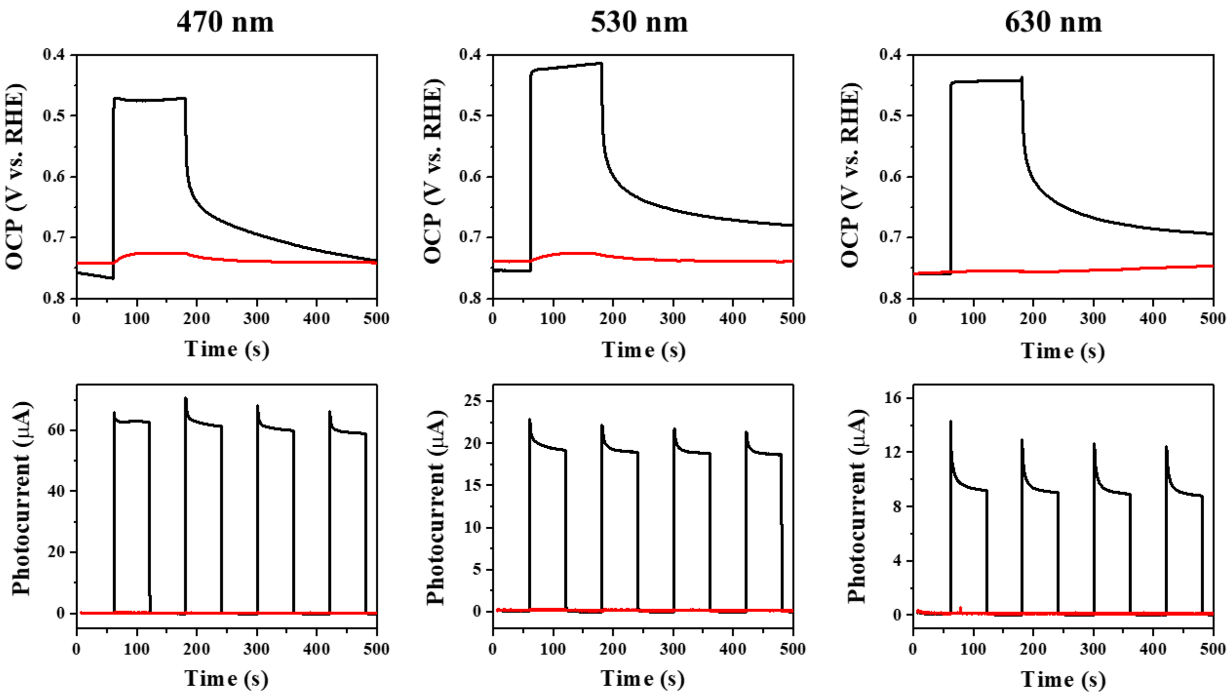

Figure S3. Comparison of photovoltage (V_{ph}, upper panel) and photocurrent (I-t) under the bias of 1.2 V_{RHE} with chopped light irradiation (lower panel) between a Au NP electrode (red lines) and a Au/TiO_2 electrode (black lines). 470 nm, 530 nm, and 630 nm LED lamps were used as irradiation sources with light intensities adjusted to 500 mW/cm^2. For the Au/TiO_2 electrode, although a higher V_{ph} was observed under 530 nm irradiation due to more intensive light absorption, the 470 nm irradiation generated a much higher photocurrent. It has been known that under 530 nm irradiation, intraband excitation mainly contributed to generation of hot holes within sp band of Au, while the 470 nm irradiation generated hot holes in d band of Au via interband transition.[4-6] Previous reports showed that those d-band holes possessed higher energy than sp-band holes[6] and were thermodynamically energetic enough to oxidize water.[4-5]

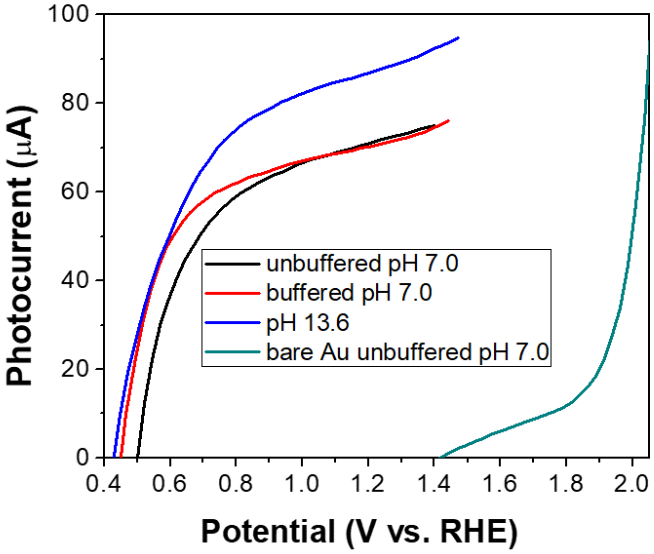

Figure S4. Linear sweep voltammetry (LSV) traces of a Au/TiO_2 electrode obtained under different pHs (7.0 and 13.6) and buffer (10 mM phosphate) conditions. The green curve was obtained from a Au NP electrode. The scan rate was 50 mV/s. The light source was a 470 nm LED lamp (500 mW/cm^2).

Supplementary Note 1. Open-circuit potential (OCP) measurement

OCP measurement was performed on a Au/TiO_2 electrode. As shown in Figure S5 and Table S1, OCP decays consisted of a fast component and a slow component.

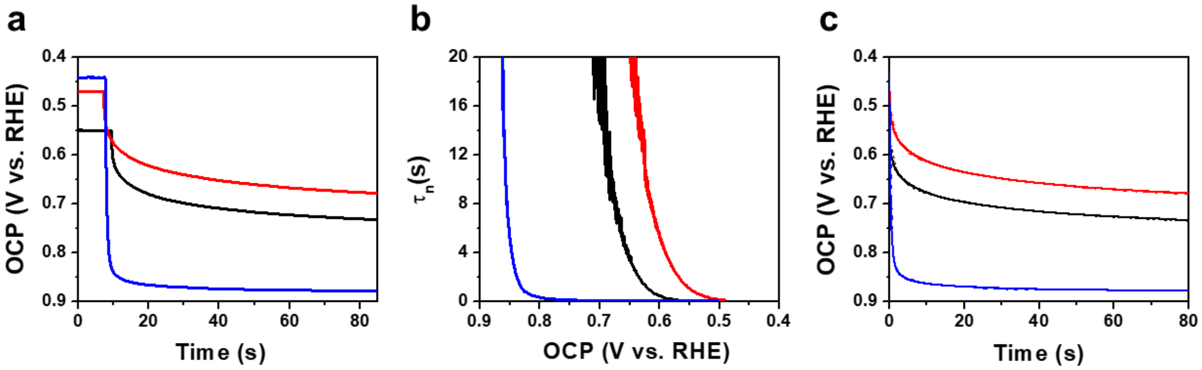

Figure S5. OCP measurements and data analysis. (**a**) OCP measurements of a Au/TiO_2 photoanode in the unbuffered solution with pH 7.0 (black) and pH 13.6 (blue) and in the buffered solution with pH 7.0 (red). The light source was a Xenon lamp coupled with a 495 nm long pass filter (300 mW/cm^2). The light was turned off at 8 s. (**b**) Calculated average lifetimes of photo-generated carriers from OCP decays. (**c**) Fitted curves of OCP decays using the exponential equation.

Average lifetimes of photo-generated carriers were calculated from OCP decays (Figure S5b) using the flowing equation:[1]

$$\tau_n = -\frac{k_B T}{q}\left(\frac{dV_{oc}}{dt}\right)^{-1}$$

where τ_n represents average lifetimes of photo-generated carriers, k_B is the Boltzmann constant, T is temperature (in Kelvin), q is the charge of an electron.

The exponential decay equation was also applied to get time constants considering that the existence of both fast and slow components of OCP decays:

$$y = y_0 + A_1 e^{-x/t_1} + A_2 e^{-x/t_2}$$

Table S1. Calculated time constants using the exponential decay equation

	y_0 (V)	A_1 (V)	t_1 (s)	A_2 (V)	t_2 (s)
unbuffered pH 7.0	0.75	-0.090	2.05	-0.085	38.74
buffered pH 7.0	0.69	-0.100	2.04	-0.100	38.34
pH 13.6	0.88	-0.400	0.44	-0.038	10.76

Supplementary Note 2. Technique issues in DWE measurements

Before sputtering a 10 nm Au film, bare FTO on Au/TiO_2 electrodes was partially coated with epoxy resin that slightly touched the Au/TiO_2 part. The remained bare FTO was fully covered with Scotch tape. After sputtering, the Scotch tape was carefully peeled off with a razor blade and this exposed FTO was used as the first working electrode connection. The second working electrode connection was made by Cu conductive tape with Ag paint connected with the Au film that covered epoxy resin (Figure S6d).

Previous DWE work emphasized that a conformal and crack-free electrocatalyst film was necessary to prevent short contact between the top Au film and bottom semiconductor substrates.[7-8] In those studies, bottom semiconductor substrates were photo-excited,[7-8] and the short contact would lead to a direct charge transfer from bottom semiconductor substrates to the top Au film. Since our research target was Au NPs, the short contact between the second working electrode Au film and the TiO_2 substrate cannot be avoided. Nonetheless, analysis of transfer of electrons and holes in the as-prepared dual-working Au/TiO_2 electrode suggested that the short contact between the Au film and TiO_2 should not be an issue for our study. As shown in Figure S6d, Au NPs and the Au film formed an Ohmic contact while both Au NPs and the Au film formed the Schottky contact with TiO_2. Since there was an Ohmic contact, Au NPs and the Au film should be considered as an integral component during photo-excitation to generate hot electrons and holes.[9] Photo-generated hot electrons were transferred to TiO_2 from both Au NPs and the Au film. It is also noted that Schottky barriers would prevent the back transfer of hot electrons from TiO_2 to either Au NPs or the Au film. Indeed, the anodic bias applied on TiO_2 generated a negligible influence on the OCP of Au in the dark (Figure S9b) while the OCP of Au moved towards the anodic direction under illumination (Figure S9b), indicating that OCP variations of Au could only be caused by hot-carrier generation rather than the applied bias on TiO_2. Taken together, for the detection of hot carriers, the short contact between the Au film and TiO_2 showed negligible influence, and the first working electrode (TiO_2) and the second working electrode (Au film) were in fact separated.

Moreover, the Au film directly sputtered on TiO_2 did not show pronounced PEC water oxidation activity (Figure S6a), indicating that the additional Au film did not generate new active sites for driving water oxidation. In general, the additional Au film should be viewed as a probe that did not change electron and hole transfer pathways in pristine Au/TiO_2 heterostructures.

A comparison of LSV traces between the pristine Au/TiO_2 electrode and the dual-working Au/TiO_2 electrode showed that PEC behaviors (onset potential and saturated photocurrent) were not remarkably affected by the additional Au film (Figure S6a). Therefore, electrochemical properties obtained from the dual-working Au/TiO_2 electrode can be used to describe the pristine Au/TiO_2 electrode.

Previous DWE studies employed back-illuminations (i.e., from FTO sides to semiconductor substrates) to avoid light absorption of the additional Au film.[8] In our study, although the sputtered Au film also had visible-light absorption (Figure S6b) and caused a decrease of 10% of the saturated photocurrent, the onset potential of PEC water oxidation on the dual-working Au/TiO_2 electrode under front-illumination remained the same as that under back-illumination (Figure S7), suggesting that active sites of water oxidation on the dual-working Au/TiO_2 electrode were not changed regardless of the illumination direction. Another concern was that due to the 3D structure of TiO_2 substrate (nanowires), back-illumination would change transfer directions of electrons and holes and make the mechanistic study more complicated. Therefore, front-illumination was used in our study to mimic conventional PEC studies of Au/TiO_2 heterostructures.

Conductivity of the second working electrode was also a critical issue that needed to be addressed in the research of DWE.[7-8] It was found that holding an additional bias on the second working electrode (the same potential was applied on the first working electrode, TiO_2, simultaneously) led to ~ 93% decrease of the photocurrent obtained from TiO_2 (by comparing Figure S6a and Figure S19a), implying that the electric field sufficiently transported to Au NPs via the Au film and counteracted the original electric field that drove electron transfer provided by the first working electrode. On the other hand, in the dark condition the potential control on Au led to the OCP variation of TiO_2 towards the same direction with similar extent (Figure S9d), further demonstrating that the second working electrode had a good conductivity, and the electric field was able to sufficiently transport to TiO_2 via the second working electrode (Au film).

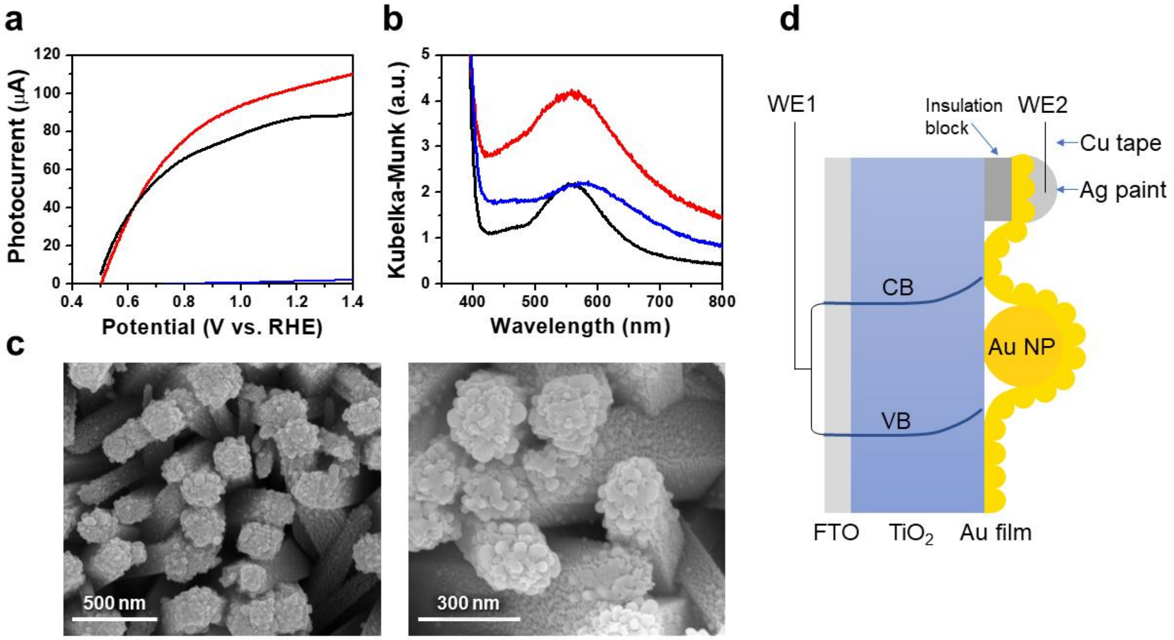

Figure S6. Characterizations and the structure of dual-working Au/TiO_2 electrodes. (**a**) LSV traces under pH 13.6 (scan rate 50 mV/s) and (**b**) UV-vis spectra of a pristine Au/TiO_2 electrode (black), a dual-working Au/TiO_2 electrode (Au film/Au/TiO_2, red) and TiO_2-Au film without Au NPs (Au film/TiO_2, blue). The light source was a 470 nm LED lamp (500 mW/cm^2). (**c**) SEM images of the dual-working Au/TiO_2 electrode. (**d**) Scheme of the dual-working Au/TiO_2 electrode. Au NPs and the Au film were considered as a whole component for photo excitation. As a result, Schottky barrier was formed between TiO_2 and the whole Au component rather than Au NPs alone. The insulation block was an epoxy resin layer. The TiO_2-Au film electrode without Au NPs showed no PEC activity. It might be the Au NP of the Au film is too small and electron transfer at interfaces is not efficient.

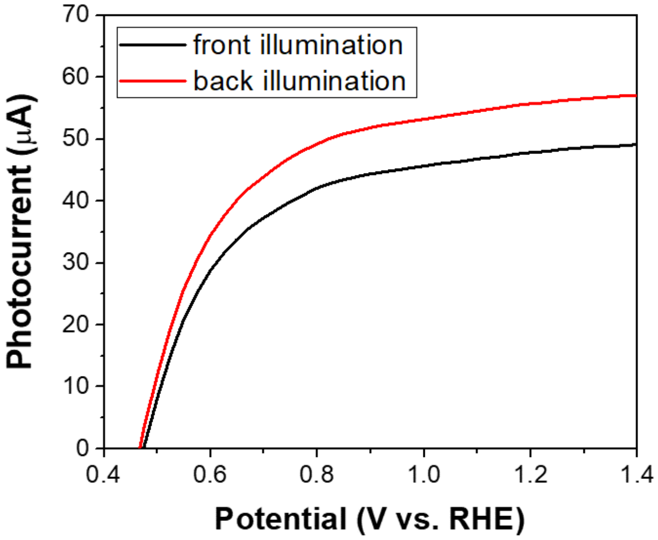

Figure S7. Comparison of LSV traces between front-illumination and back-illumination on a dual-working Au/TiO$_2$ electrode. The light source was a 470 nm LED lamp (500 mW/cm^2). The scan rate was 50 mV/s.

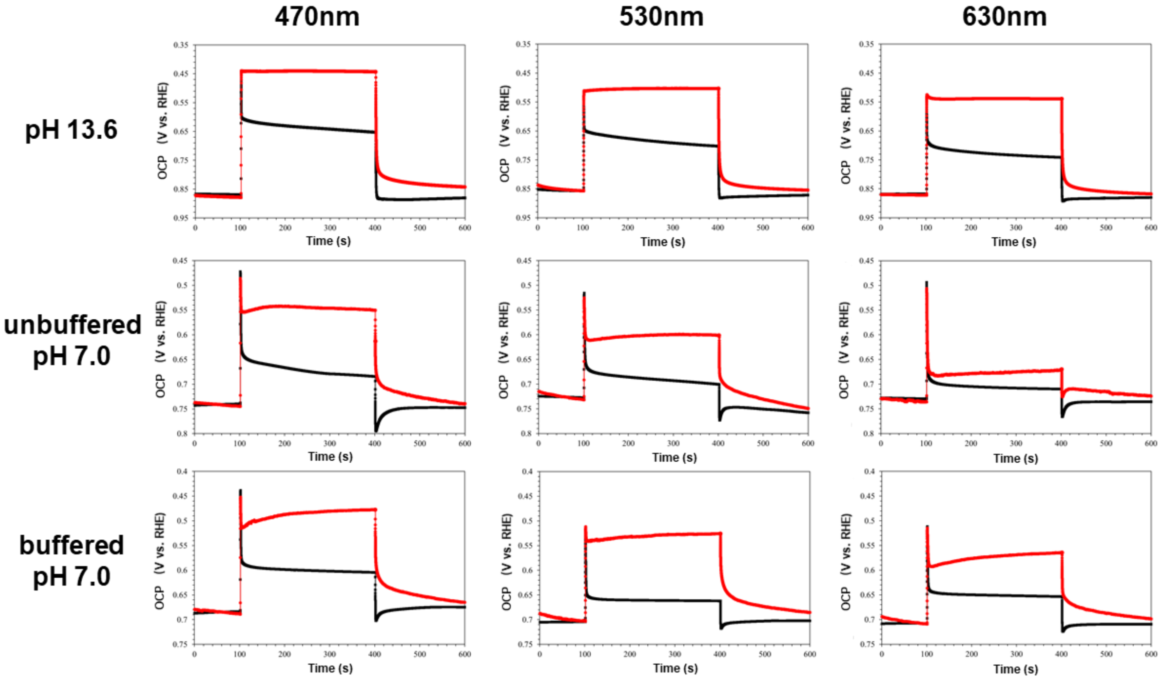

Figure S8. V_{ph} on a dual-working Au/TiO_2 electrode: data obtained from TiO_2 (red) and Au (black). Experiments were performed under three solution conditions (unbuffered pH 7.0, buffered pH 7.0, and pH 13.6) using three light sources (470 nm, 530 nm, and 630 nm LED lamps) with light intensities adjusted to 500 mW/cm^2. The OCP of Au was manually shifted to align the dark OCP of Au with that of TiO_2 for comparison.

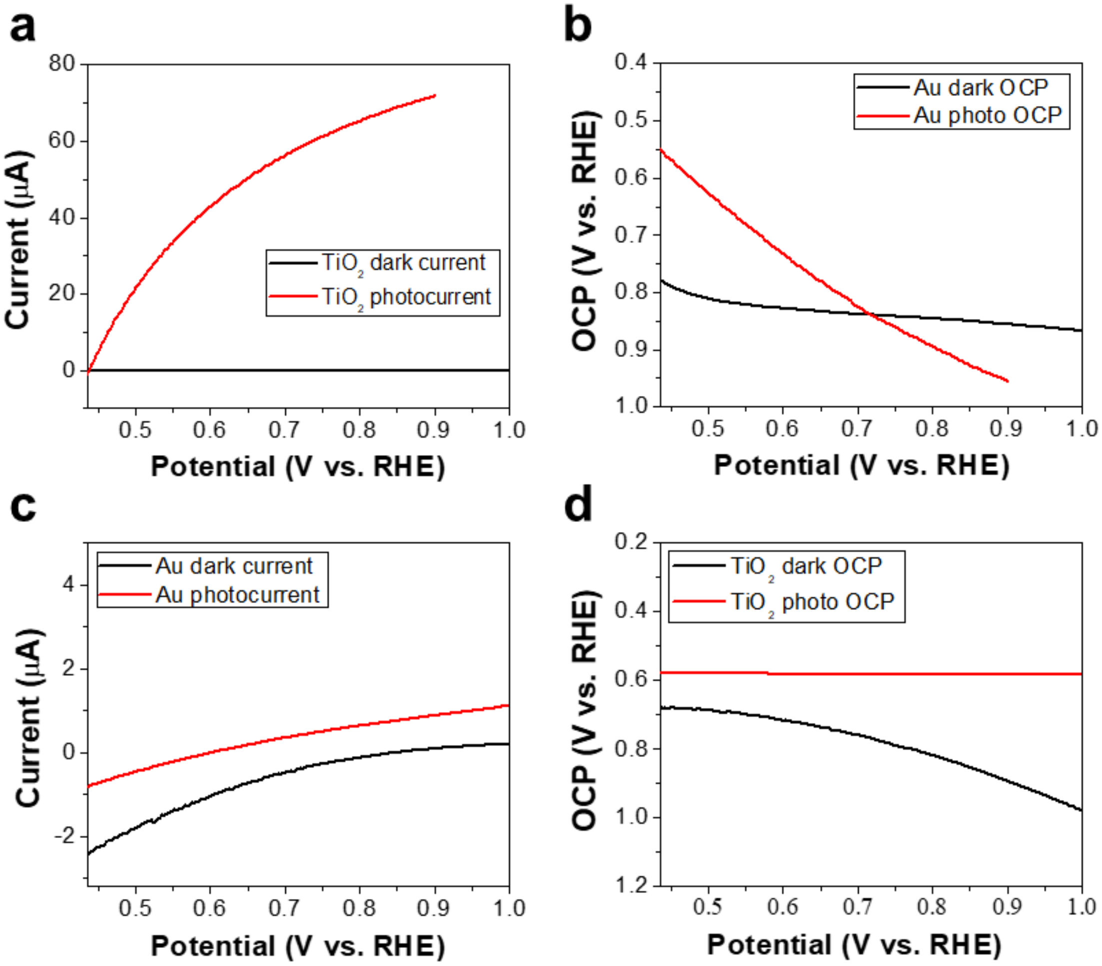

Figure S9. in situ OCP measurements during LSV on a dual-working Au/TiO$_2$ electrode. (**a**) LSV measurements were performed on TiO$_2$ and (**b**) OCP of Au was monitored simultaneously. (**c**) LSV measurements were performed on Au and (**d**) OCP of TiO$_2$ was monitored simultaneously. The scan rate was 1 mV/s. The light source was a 470 nm LED lamp (500 mW/cm^2).

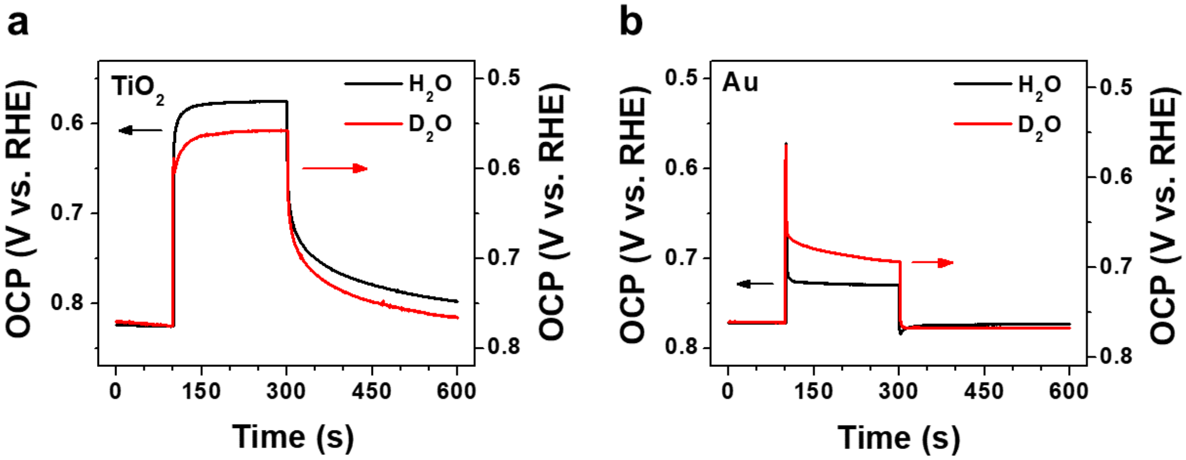

Figure S10. Isotope effect of V_{ph} obtained from a dual-working Au/TiO_2 electrode in the unbuffered solution with pH 7.0: data obtained from (**a**) TiO_2 and (**b**) Au. The light was turned on at 100 s and off at 300 s.

Supplementary Note 3. Electrochemical impedance spectroscopy (EIS)

Surface-trapped holes on a Au/TiO_2 photoanode under PEC water oxidation was investigated by fitting and simulating EIS data using a well-developed electric model. As shown in Figure S11, R_s stands for the series resistance, C_{bulk} represents the capacitance of Helmholtz layer and depletion region on the surface of electrodes, $R_{trapping}$ represents the resistance of hole trapping process at surface states, C_{trap} represents the amount of surface-trapped holes, and $R_{ct,trap}$ represents the resistance of charge transfer across the interface.[2, 10] The fitted parameters were listed in Figure S12, Table S2 and S3.

The series resistance R_s was a constant (~ 10 Ω as shown in Table S2) under various mono-wavelength irradiations and applied potentials, indicating that the fitting and simulation process was reliable for Au/TiO_2.[11] C_{trap} decreased with the applied bias while $R_{ct,trap}$ increased with the applied bias (Figure S12), implying the discharging of surface states (i.e., releasing of surface trapped holes) proceeded with water oxidation.[2, 10, 12-13] The amount of surface-trapped holes (C_{trap}) was larger in the unbuffered solution with pH 7.0 than that in the buffered solution with pH 7.0 and pH 13.6 (Figure S13a). Since C_{trap} was a balance between the hole trapping process and the hole releasing process,[2, 13] the larger C_{trap} suggested that the surface trapped holes were not able to sufficiently transfer to water molecules under the unbuffered pH 7.0 condition as those under the buffered pH 7.0 and pH 13.6 conditions.

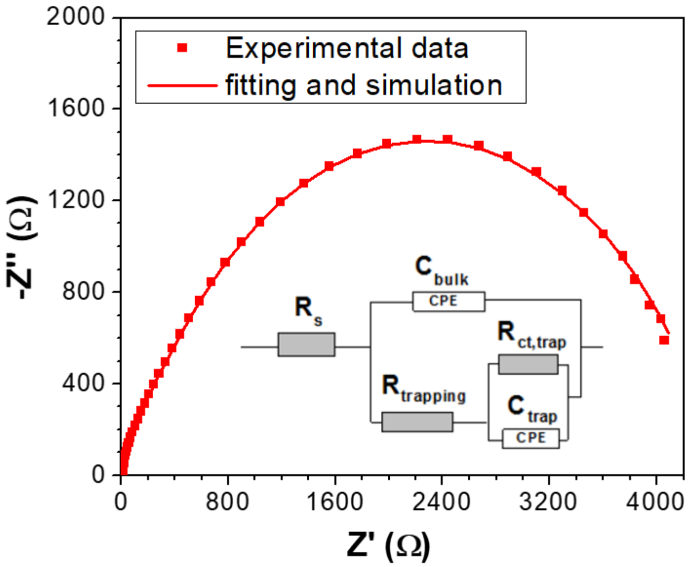

Figure S11. A representative Nyquist plot obtained from the EIS measurement of a Au/TiO$_2$ electrode at 0.5 V$_{RHE}$ under pH 13.6. Inset was the model circuit used for fitting and simulation.

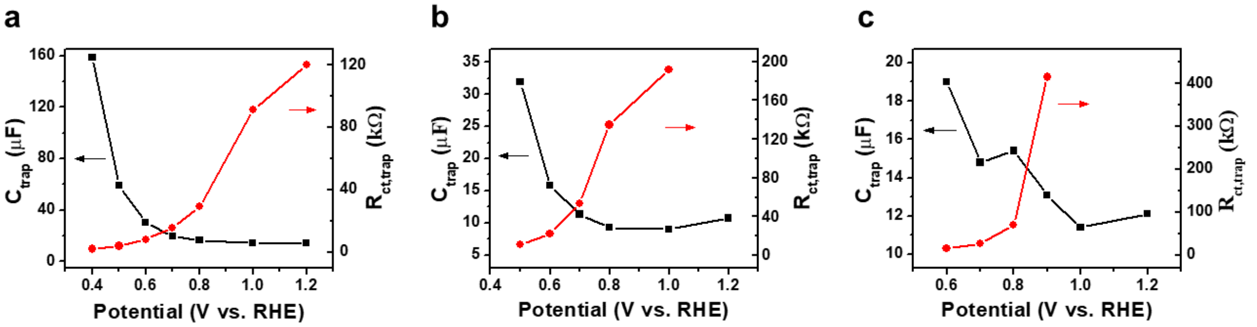

Figure S12. Calculated EIS parameters under various irradiations. C_{trap} and $R_{ct,trap}$ calculated from the fitting and simulation of EIS data obtained under various applied potentials in the solution with pH 13.6 with three irradiation wavelengths: (**a**) 470 nm; (**b**) 530 nm; (**C**) 630 nm.

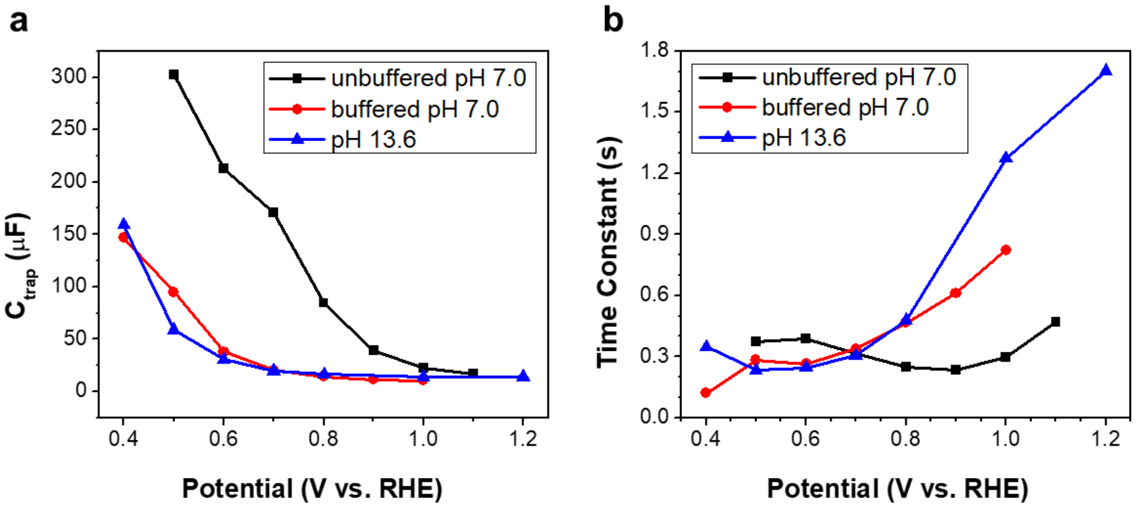

Figure S13. Calculated EIS parameters in various electrolytes. (**a**) C_{trap} and (**b**) time constants of charging and discharging of surface states calculated from the fitting and simulation of EIS spectra. All experiments were performed using a 470 nm LED lamp (500 mW/cm^2).

Table S2. Parameters calculated from EIS data obtained under various illuminations

Wavelength	Potential (V_{RHE})	R_s (Ω)	C_H (μF)	$R_{trapping}$ (Ω)	$R_{ct,trap}$ (Ω)	C_{trap} (μF)	T_{trap} (s)
470 nm	0.4	10.6	13.2	419	2190	159.0	0.34
	0.5	10.5	11.5	531	3940	59.0	0.23
	0.6	10.4	11.6	707	8060	30.4	0.24
	0.7	10.3	11.6	949	15600	19.5	0.30
	0.8	10.3	10.9	928	29200	16.4	0.48
	1.0	10.3	10.2	622	91500	13.9	1.27
	1.2	10.3	10.4	508	120000	14.2	1.70
530 nm	0.5	10.5	11.1	1860	10700	31.9	0.34
	0.6	10.4	10.9	2810	22300	15.8	0.35
	0.7	10.4	10.7	3700	53600	11.3	0.60
	0.8	10.4	10.6	5260	135000	9.3	1.25
	1.0	10.4	10.4	5060	192000	9.0	1.72
	1.2	10.4	10.7	6060	——	10.7	——
630 nm	0.6	9.1	11.4	1720	15300	19.0	0.29
	0.7	9.2	10.8	3030	26900	14.8	0.39
	0.8	9.2	10.4	3880	70300	15.4	1.08
	0.9	9.3	10.1	3380	416000	13.1	5.40
	1.0	9.3	10.2	4390	——	11.4	——
	1.2	9.3	10.5	6870	——	12.1	——

Table S3. Parameters calculated from EIS data obtained under various electrolyte conditions

	Potential (V_{RHE})	R_s (Ω)	C_H (μF)	$R_{trapping}$ (Ω)	$R_{ct,trap}$ (Ω)	C_{trap} (μF)	T_{trap} (s)
Unbuffered pH 7.0	0.5	17.4	11.7	297	1240	302.0	0.37
	0.6	17.2	11.3	326	1830	213.0	0.39
	0.7	17.2	10.7	363	1860	171.0	0.32
	0.8	17.1	10.3	408	2950	84.4	0.25
	0.9	17.0	11.3	583	5920	39.4	0.23
	1.0	16.8	12.3	996	13600	22.0	0.30
	1.1	16.8	11.8	1320	28200	16.7	0.47
Buffered pH 7.0	0.4	29.3	16.1	399	817	147.0	0.12
	0.5	28.9	13.5	480	2990	94.7	0.28
	0.6	28.4	13.8	796	6920	38.2	0.26
	0.7	28.0	13.7	1330	16600	20.4	0.34
	0.8	27.9	13.4	2070	32900	14.2	0.47
	0.9	27.7	13.1	3310	53100	11.5	0.61
	1.0	27.5	12.6	4700	76100	10.8	0.82
pH 13.6	0.4	10.6	13.2	419	2190	159.0	0.35
	0.5	10.5	11.5	531	3940	59.0	0.23
	0.6	10.4	11.6	707	8060	30.4	0.25
	0.7	10.3	11.6	949	15600	19.5	0.30
	0.8	10.3	10.9	928	29200	16.4	0.48
	1.0	10.3	10.2	622	91500	13.9	1.27
	1.2	10.3	10.4	508	120000	14.2	1.70

Supplementary Note 4. Equations for reaction order analysis

Under steady state, the water-oxidation rate (photocurrent density, J in μA/cm^2) is related to the surface hole density ([hole] in nm^{-2}) as:[14-15]

$$\mathrm{J} = \mathrm{k_{WO}}[\mathrm{holes}]^{\beta}$$

$$\mathrm{Log\,J} = \beta\log([\mathrm{holes}]) + \log\mathrm{k_{WO}}$$

Where k_{wo} is the water oxidation rate constant, and β is the reaction order of surface trapped holes.

Surface hole density was calculated from EIS results based on the model circuit displayed in Figure S11 and by the following equation:[15]

$$[\mathrm{hole}] = \mathrm{C_{trap}} * \mathrm{V_{appl}} * \frac{\mathrm{R_{ct,trap}}}{\mathrm{R_s} + \mathrm{R_{trapping}} + \mathrm{R_{ct,trap}}} * S^{-1}$$

where V_{appl} is the applied potential and S is the active area of electrodes.

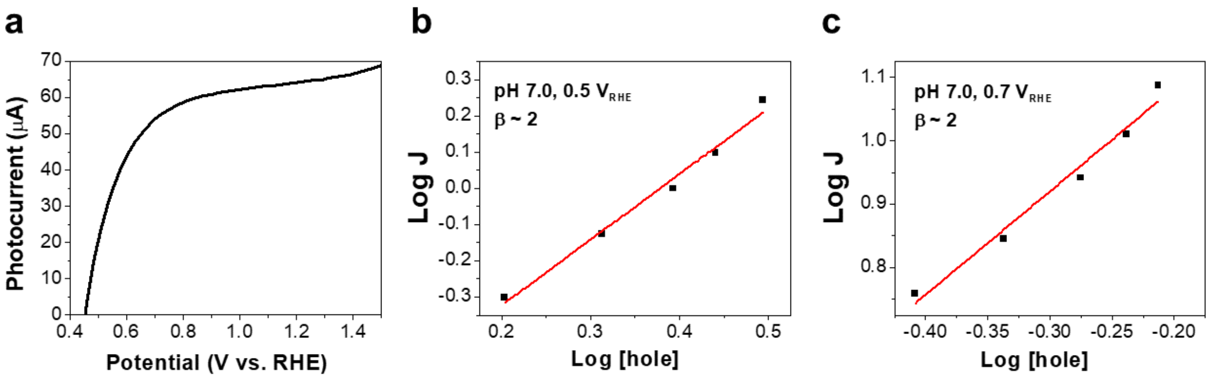

Figure S14. Rate law analysis of PEC water oxidation on Au/TiO$_2$ in the unbuffered solution with pH 7.0. (**a**) The LSV trace. Relationship between photocurrent densities and surface hole densities of a Au/TiO$_2$ photoanode at (**b**) 0.5 V$_{RHE}$ and (**c**) 0.7 V$_{RHE}$.

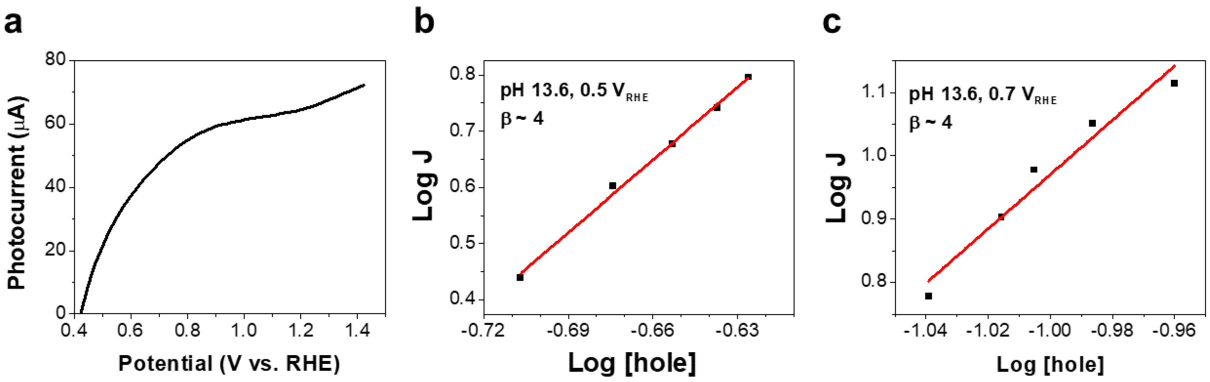

Figure S15. Rate law analysis of PEC water oxidation on Au/TiO₂ under pH 13.6. (**a**) The LSV trace. Relationship between photocurrent densities and surface hole densities of a Au/TiO₂ photoanode at (**b**) 0.5 V_{RHE} and (**c**) 0.7 V_{RHE}.

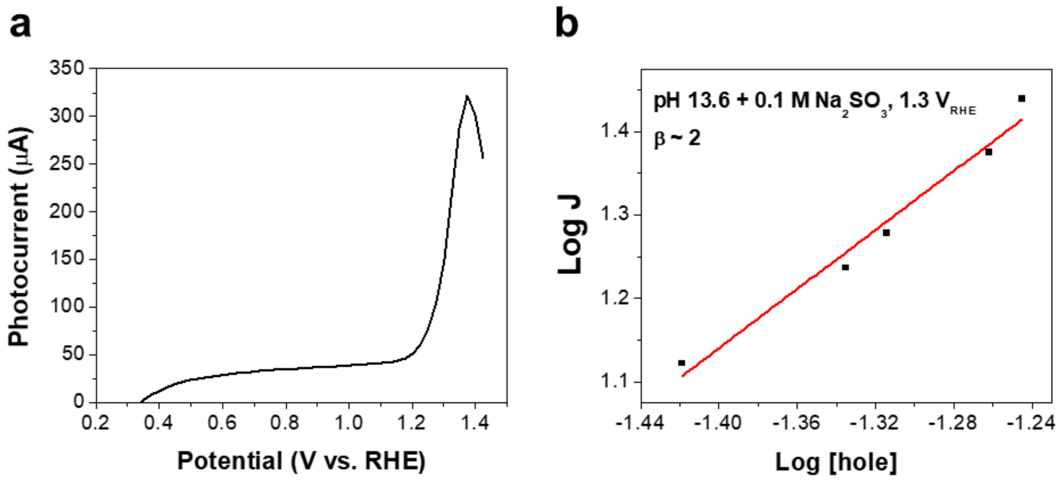

Figure S16. Rate law analysis of oxidation of Na_2SO_3 on Au/TiO_2 under pH 13.6. (**a**) The LSV trace. (**b**) Relationship between photocurrent densities and surface hole densities of a Au/TiO_2 photoanode at 1.3 V_{RHE}; 1.3 V_{RHE} was used to ensure efficient oxidation of Na_2SO_3. Na_2SO_3 was used as a hole scavenger to diminish the barrier of surface chemical reactions and leave only hole-trapping steps in RDS. It was observed that Na_2SO_3 decreased the reaction order from ~ 4 to ~ 2, confirming the formation of two adjacent trapped holes in RDS under alkaline conditions.

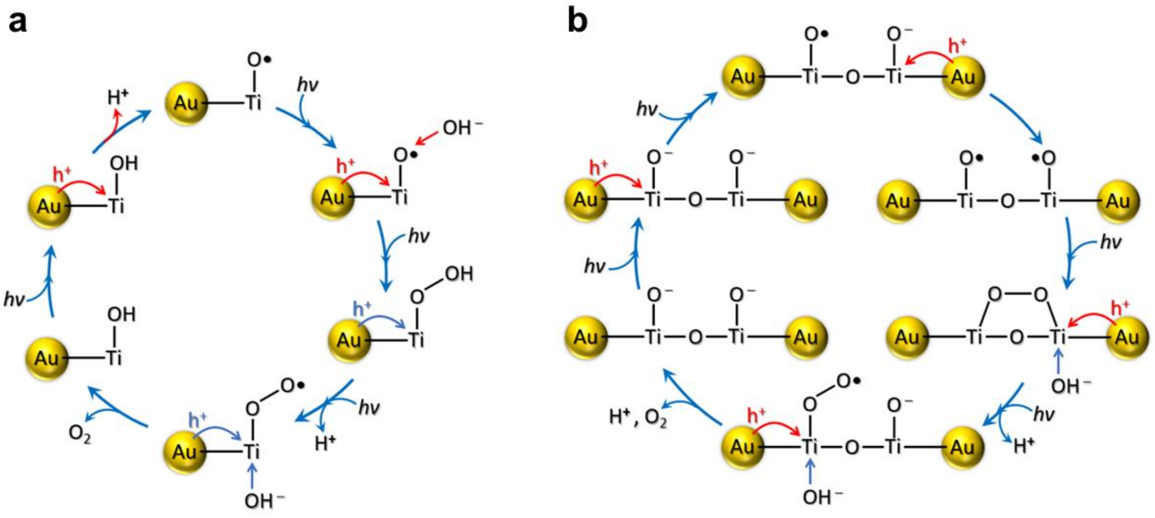

Figure S17. Scheme of hole transfer and water oxidation on Au/TiO_2 heterostructures under (a) neutral and (b) alkaline conditions. Red arrows represent hole transfer in RDS. Surface-trapped holes were proposed to be stored in terminal oxygens in the form of Ti-O·. In previous studies, both terminal and the bridging oxygens were proposed to be active sites for trapping photo-generated holes on TiO_2.[16-19] However, as the bridging oxygen exhibited much higher acidity (pK_a below 0) than the terminal oxygen ($pK_a \sim 9$) on rutile TiO_2 surfaces,[20] the deprotonation process should be absent on Ti-O-Ti and Ti-O-Au structures under pH 7.0 – 13.6 conditions. Therefore, the terminal oxygen (-Ti-OH) was more likely to be the hole-trapping site that accounted for the observed isotopic effect in Figure S10.

Table S4. Parameters calculated from EIS data obtained under various electrolyte conditions for rate law analysis

	Light intensity (mW·cm^{-2})	R_s (Ω)	$R_{trapping}$ (Ω)	C_H (μF)	$R_{ct,trap}$ (Ω)	C_{trap} (μF)	[hole] (nm^{-2})	log [hole]	J (μA·cm^{-2})	log J
pH 7.0 0.5 V_{RHE}	500	26.5	240	9.6	5320	420.0	3.120	0.494	1.75	0.243
	453	26.5	250	9.7	4800	374.0	2.758	0.441	1.25	0.097
	402	26.5	263	9.7	5140	335.0	2.474	0.393	1.00	0.000
	345	26.4	295	9.6	5080	280.0	2.054	0.313	0.75	-0.125
	277	26.4	354	9.5	5110	220.0	1.597	0.203	0.50	-0.301
pH 7.0 0.7 V_{RHE}	500	26.4	352	8.9	3380	61.9	0.612	-0.213	12.25	1.088
	453	26.3	369	9.1	3580	58.3	0.578	-0.238	10.25	1.011
	402	26.3	418	9.3	3970	53.6	0.530	-0.276	8.75	0.942
	345	26.4	503	9.4	4700	46.5	0.460	-0.338	7.00	0.845
	277	26.4	635	9.4	6000	39.4	0.390	-0.409	5.75	0.760
pH 13.6 0.5 V_{RHE}	500	15.6	692	11.3	4480	35.1	0.236	-0.626	6.25	0.796
	453	15.6	717	11.4	4880	34.0	0.231	-0.637	5.50	0.740
	402	15.5	786	11.3	5300	32.8	0.222	-0.653	4.75	0.677
	345	15.6	878	11.1	5850	31.3	0.212	-0.674	4.00	0.602
	277	15.6	1010	10.9	6580	29.1	0.196	-0.707	2.75	0.439
pH 13.6 0.7 V_{RHE}	500	18.9	1300	10.5	11600	11.1	0.110	-0.960	13.00	1.114
	453	18.9	1340	10.6	12500	10.4	0.103	-0.986	11.25	1.051
	402	18.9	1450	10.5	13000	10.0	0.099	-1.005	9.50	0.978
	345	18.9	1600	10.3	13500	9.8	0.096	-1.016	8.00	0.903
	277	18.9	1960	10.2	13900	9.5	0.091	-1.039	6.00	0.778
pH 13.6 Na_2SO_3 1.3 V_{RHE}	500	16.9	871	12.2	115	24.8	0.057	-1.245	27.50	1.439
	453	16.8	854	11.7	125	21.8	0.055	-1.262	23.75	1.376
	402	16.9	918	11.0	161	16.5	0.048	-1.314	19.00	1.279
	345	16.9	1010	10.6	166	16.6	0.046	-1.335	17.25	1.237
	277	16.9	1140	10.1	212	12.3	0.038	-1.419	13.25	1.122

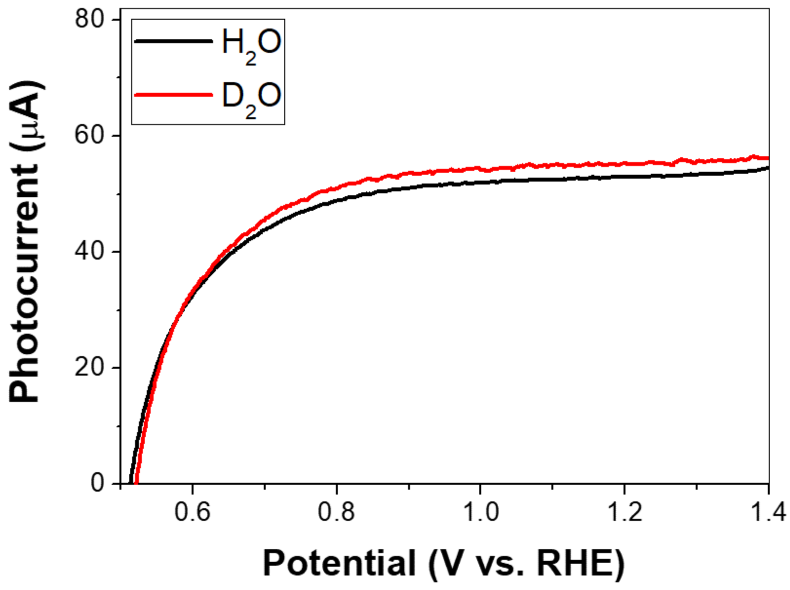

Figure S18. H/D kinetic isotope effect (KIE) measurement on a Au/TiO$_2$ photoanode under pH/pD 7.0. The experiments were performed under the irradiation using an Xe lamp coupled with a 495 nm long pass filter.

H/D kinetic isotope effect (KIE) experiment was performed to further confirm whether H_2O molecules could be oxidized by hot holes, as oxidation of H_2O molecules would lead to a pronounced KIE according to the previous PEC water oxidation research on semiconductors.[2] LSV curves of the Au/TiO$_2$ photoanode exhibited no significant difference between H_2O and D_2O under pH/pD 7.0, excluding the possibility to have the O-H bond cleavage in RDS. Therefore, the oxidation of H_2O molecules should not be the major contribution to PEC activities. Instead, the oxidation of OH^- contributed to observed PEC activities in our work.

The Fermi level of Au is located ~0.3 V more cathodic than the redox potential of O_2/H_2O.[5] Considering that photo-generated hot holes on metals quickly relax to the Fermi level before chemical reactions occur,[22] those photo-generated holes are not able to directly drive the oxidation of H_2O molecules. Hence, it is reasonable that the oxidation of OH^- mainly contributes to PEC activities.

Supplementary Note 5. Simultaneous photocurrent measurement of dual-working Au/TiO_2 electrodes

Simultaneous photocurrent measurement was performed on Au and TiO_2 of a dual-working Au/TiO_2 electrode to study the electron transfer dynamics under quasi open-circuit conditions. Constant potentials were simultaneously applied on TiO_2 and Au, and the electric force applied on TiO_2 was offset from that on Au to mimic open-circuit conditions while still generated photocurrents on both TiO_2 and Au. The photocurrent obtained from TiO_2 was reduced by ~ 93% (5 μA, Figure S19a) compared to that under closed-circuit conditions (70 μA, Figure S20). Under open-circuit conditions, hot electrons generated on Au via interband transitions could hardly be transferred to TiO_2 since there was no electric field driving them towards TiO_2. Instead, hot electrons tended to recombine with hot holes on Au[21] and this recombination accounted for the ~ 93% loss of photocurrent under open-circuit conditions compared to that under closed-circuit conditions.

It is noted that under quasi open-circuit conditions, the photocurrent on TiO_2 was about two orders of magnitude higher than that on Au (under 470 nm irradiation in Figure S19 and under 530 and 630 nm irradiation in Figure S22). However, Figure S21 showed that without Au NPs (i.e., TiO_2-Au film electrode), the photocurrent obtained from TiO_2 was the same as that obtained from Au, indicating that the observed photocurrent difference (Figure S19) was caused by the photo-excitation of Au NPs. We further demonstrated that photocurrents of TiO_2 did not change with the applied bias on Au (Figure S19). All these results suggested the existence of a direct electron transfer mechanism, in which the photoexcitation of Au directly led to generation of hot electrons in the conduction band of TiO_2.[22-23] Direct electron transfer in metal/semiconductor photocatalysts has been demonstrated to be an ultrafast process.[23] Since hot-hole transfer from Au to TiO_2 was found to be a proton-coupled process (Figure S10), the mismatch of timescales of those two processes suppressed electron-hole recombination on TiO_2, which contributed to the substantial V_{ph} obtained on Au/TiO_2 heterostructures (Figure S5 and Figure S8).

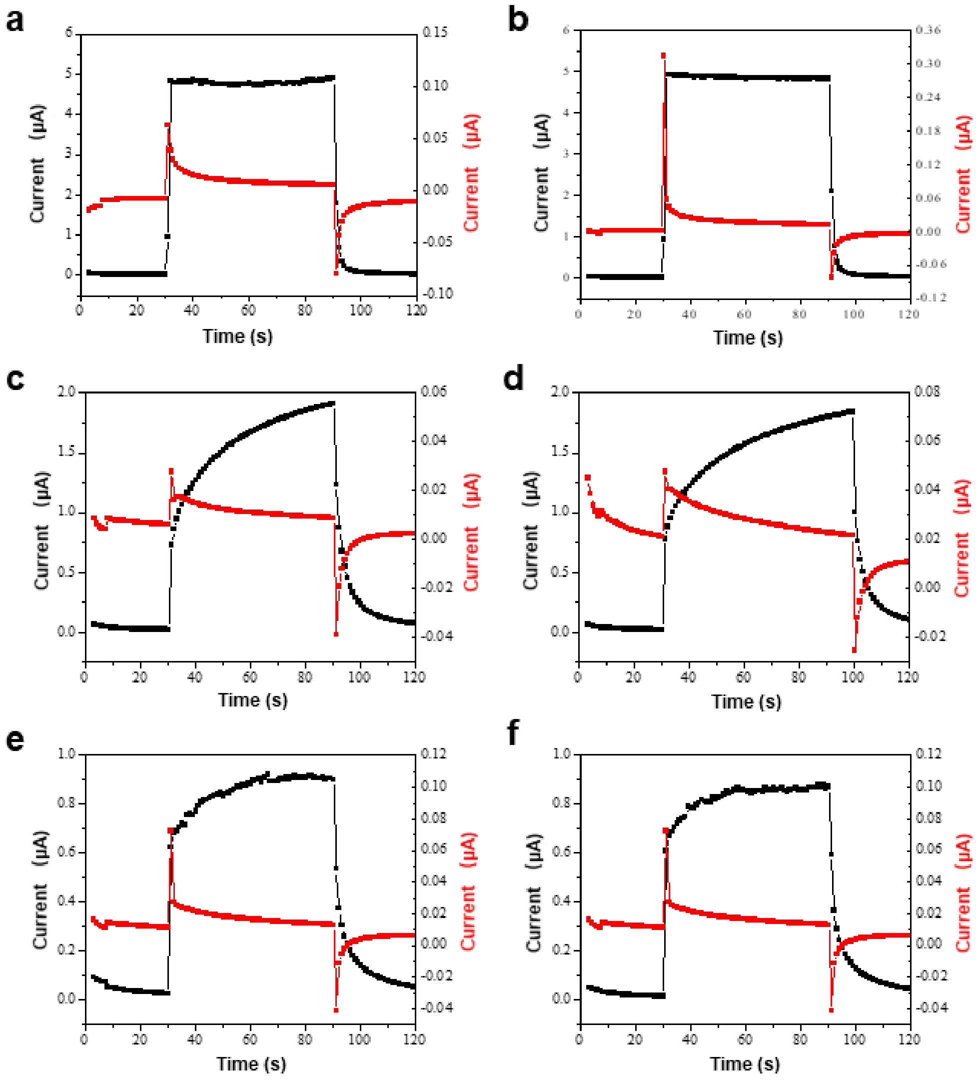

Figure S19. Photocurrent on a dual-working Au/TiO_2 electrode with constant potentials on TiO_2 (black lines) and Au (red lines) in solutions with: (**a, b**) pH 13.6, (**c, d**) pH 7.0 (buffered), and (**e, f**) pH 7.0 (unbuffered). The applied potential on TiO_2 was 0.8 V_{RHE}, while applied potentials on Au were 0.8 V_{RHE} (**a, c, e**) and 1.0 V_{RHE} (**b, d, f**). The light source was a 470 nm LED lamp (500 mW/cm^2). The light was turned on at 30 s and off at 90 s.

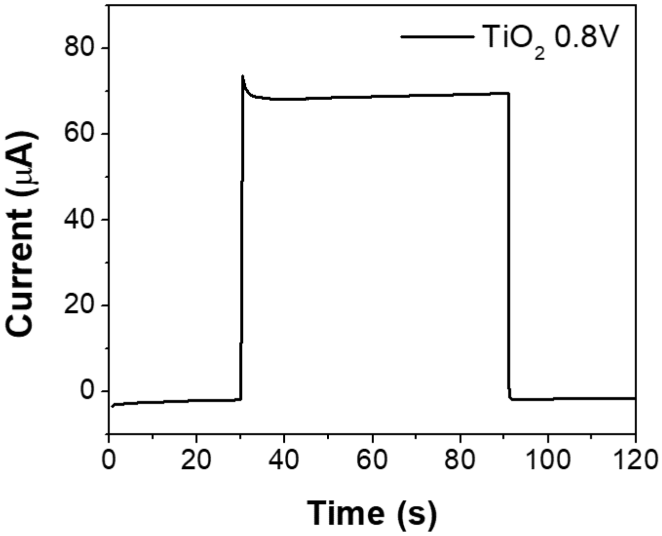

Figure S20. Photocurrent on a dual-working Au/TiO$_2$ electrode with a potential of 0.8 V$_{RHE}$ on TiO$_2$ while leaving Au under open-circuit conditions (pH 13.6). The light source was a 470 nm LED lamp (500 mW/cm^2). The light was turned on at 30 s and off at 90 s.

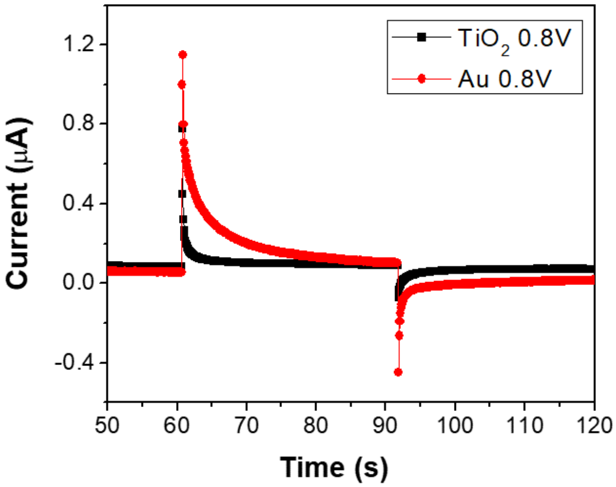

Figure S21. Photocurrent on a TiO_2-Au film electrode without Au NPs. A constant potential ($0.8V_{RHE}$) was applied on both TiO_2 and Au in the solution with pH 13.6. The light source was a 470 nm LED lamp (500 mW/cm^2). The light was turned on at 60 s and off at 92 s.

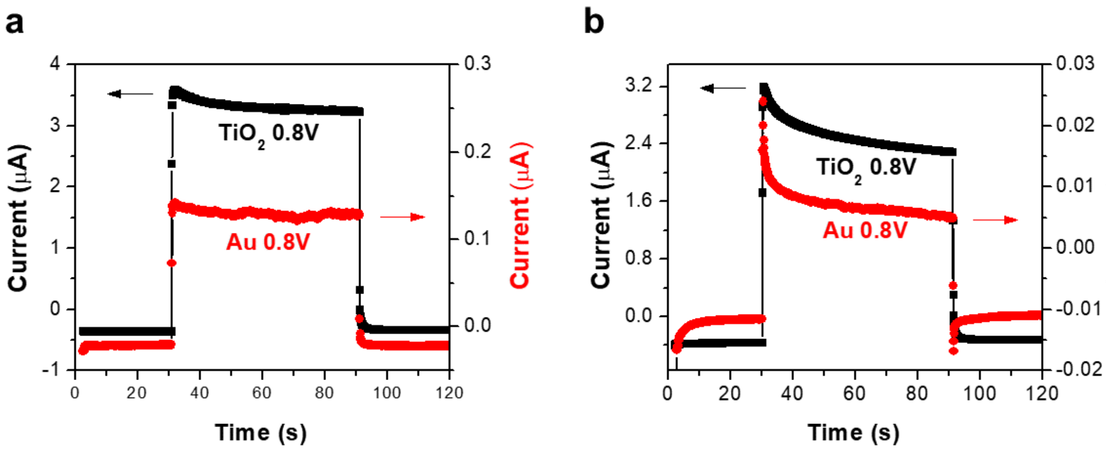

Figure S22. Photocurrent on a dual-working Au/TiO$_2$ electrode. A constant potential (0.8 V_{RHE}) was applied on TiO$_2$ (black lines) and Au (red lines) in the solution with pH 13.6. The irradiations were (**a**) 530 nm LED lamp and (**b**) 630 nm LED lamp (500 mW/cm^2). The light was turned on at 30 s and off at 90 s.

Supplementary Note 6. Preparation of catechol-modified Au/TiO_2 electrodes

Catechol was photoelectrodeposited on Au/TiO_2 heterostructures under 1.0 V_{RHE} and 470 nm irradiation for 240 s (Figure S23). After the deposition, the electrode was moved to a clean electrolyte (0.1 M $NaClO_4$ with pH 7.0) without catechol and fully charged with hot holes under 1.2 V_{RHE} and 470 nm irradiation for 1 h (Figure S24). Also, photodeposition (i.e., without applied bias) was used to selectively deposit catechol only on Au of Au/TiO_2 heterostructures (Figure S25). Without bias, the oligomerization of catechol on Au/TiO_2 was slow and thus a much longer irradiation time was needed (10 h).

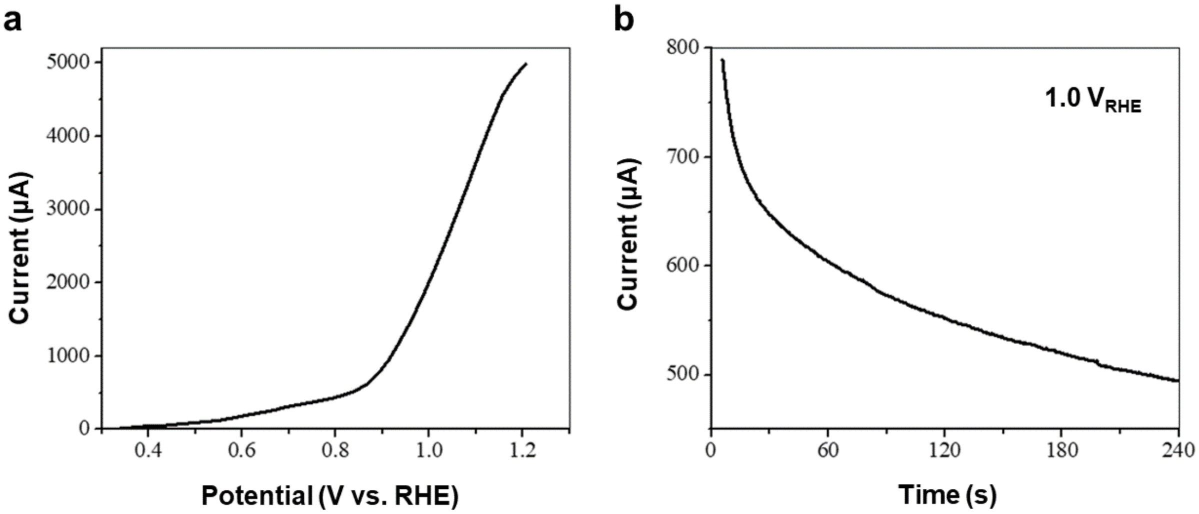

Figure S23. Photoelectrodeposition of catechol on a Au/TiO_2 electrode. (**a**) LSV measurement of a Au/TiO_2 electrode in the solution containing catechol (0.1 M). (**b**) Chronoamperometry performed at 1.0 V_{RHE} for 240 s. The light source was a 470 nm LED lamp (500 mW/cm^2).

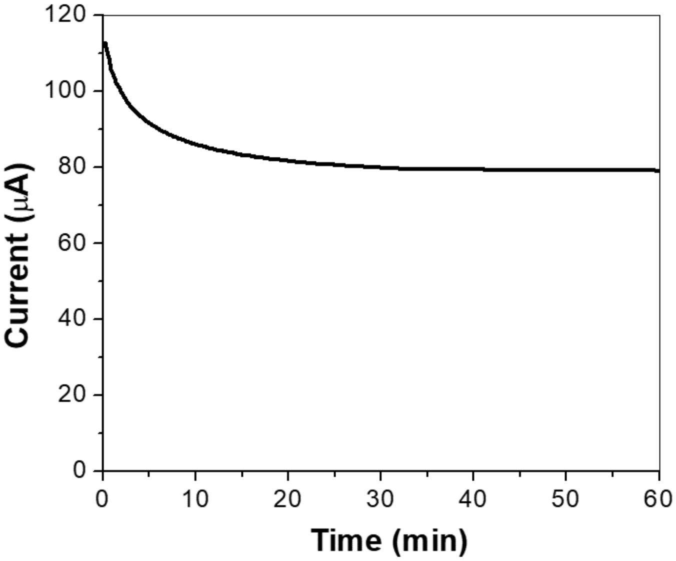

Figure S24. Charging of the catechol-modified Au/TiO_2 electrode. A constant potential of 1.2 V_{RHE} was held on the catechol-modified Au/TiO_2 electrode under 470 nm irradiation (500 mW/cm^2) for 1 h to fully charge the electrode with hot holes. The photocurrent eventually reached a plateau, indicating that all hydroxyl groups were oxidized to ketone groups.

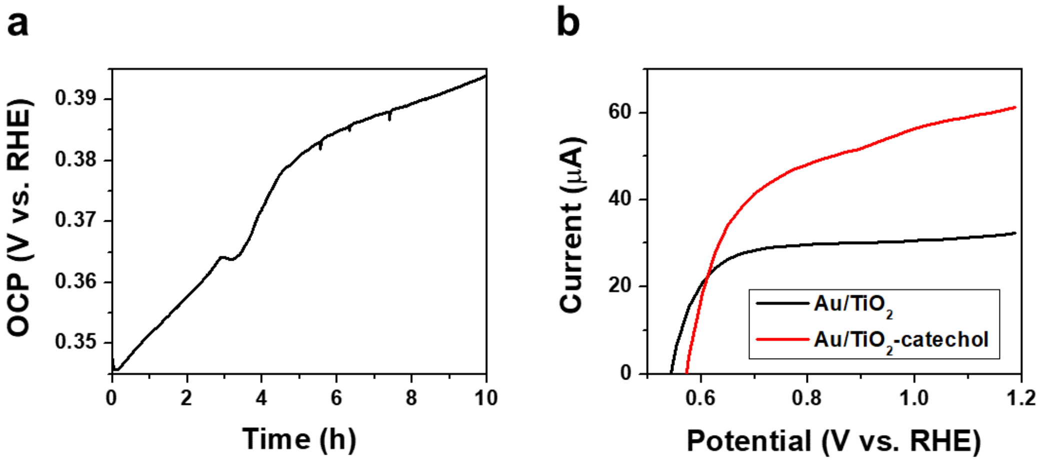

Figure S25. Photodeposition of catechol on a Au/TiO_2 electrode. (**a**) OCP measurement of a Au/TiO_2 electrode in the solution containing catechol (0.1 M) under 470 nm irradiation for 10 h. (**b**) LSV measurements on the pristine and catechol-modified Au/TiO_2 electrodes. The light source was a 470 nm LED lamp (500 mW/cm^2).

Table S5. Molecular weight (MW) of oligo-catechol obtained from LC-MS.

	oligo-catechol		**catechol control**		
MW	**Retention time (RT) (min)**	**Total Area**	**RT (min)**	**Total Area**	$\frac{\mathbf{oligo-catechol}}{\mathbf{catechol\ control}}$
MW 218	19.78	144,385,064	19.82	1,827,528	79.01
MW 218	22.58	80,669,676	22.61	2,067,386	39.02
m/z 443 ion	23.92	1,873,403	nd*		
MW 218	25.45	107,152,534	25.45	2,566,451	41.75
MW 218	25.90	15,132,772	nd		
MW 218	28.17	1,153,760	28.18	775,180	1.49
MW 326	23.92	9,714,149	nd		
MW 216	34.12	6,176,494	nd		

nd*: not detected.

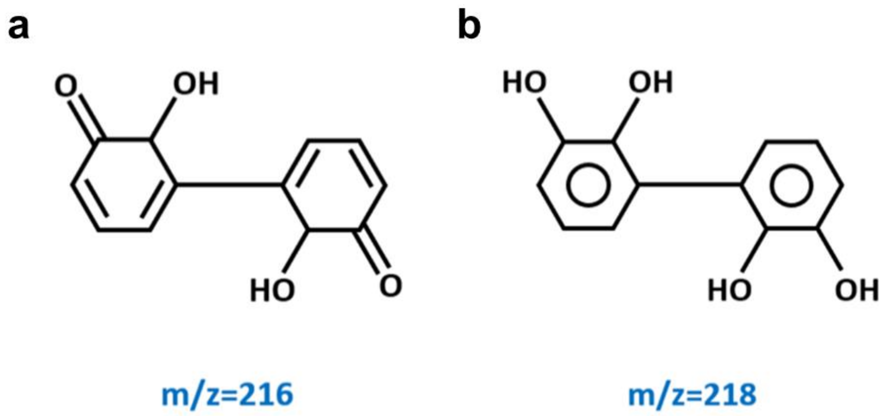

Figure S26. Molecular structures of oligo-catechol. The appearance of (**a**) m/z-2 species (m/z 216 compared with m/z 218 in Table S5) demonstrated that (**b**) catechol dimer further trapped hot holes via a one-hole process of oxidizing hydroxyl groups (-C-OH) to ketone groups (-C=O). The stable semiquinone species (m/z=216) also indicated that the semiquinone possessed low oxidative capability that was hard to fully release trapped holes to return to the original state of catechol. It is noted that the LC-MS experiment was an ex situ technique. In fact, it has been previously reported that the redox process among quinone, semiquinone and hydroquinone functioned to trap and release holes in photocatalysis.[25] Observation of semiquinone was achieved by EPR studies.[25]

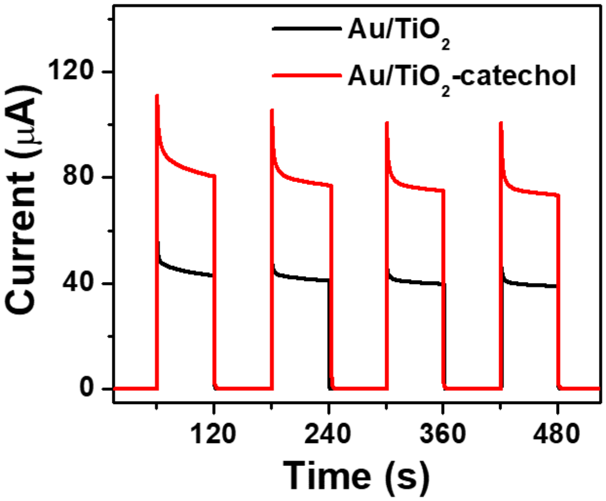

Figure S27. Chronoamperometry performed on the pristine Au/TiO$_2$ electrode (black) and catechol-modified Au/TiO$_2$ electrode (red) at 1.2 V$_{RHE}$ under chopped-light irradiation. The light source was a 470 nm LED lamp (500 mW/cm^2). The pristine Au/TiO$_2$ electrode generated a steady photocurrent of 39 μA while the catechol-modified Au/TiO$_2$ electrode generated a steady photocurrent of 73 μA. Therefore, the enhancement factor was (73-39)/39 = 87%.

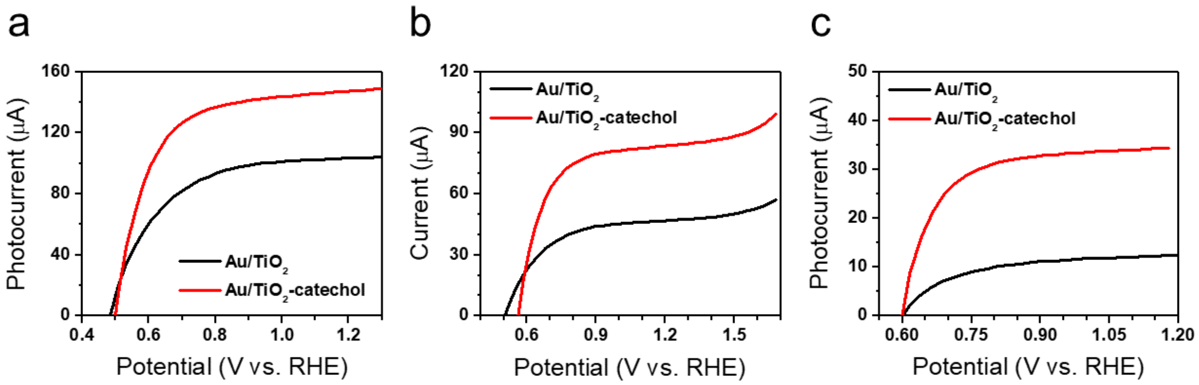

Figure S28. The reproducibility of catechol-mediated photocurrent enhancement. The catechol modification and the relevant PEC measurements were repeated for several times and here we show three representative cases. The activity enhancement caused by catechol modification depends on the original activity of Au/TiO_2 electrodes. When the activity of bare Au/TiO_2 electrodes is high (figure a), it showed relatively low enhancement factor (from 103 uA to 147 uA, enhanced by 43%). Figure b (i.e., Figure 2a in the manuscript) showed the moderate activity of bare Au/TiO_2 electrode and accordingly the moderate enhancement factor (from 47 uA to 84 uA, enhanced by 80%). Figure c showed the lowest activity of bare Au/TiO_2 electrode but the highest enhancement factor (from 12 uA to 34 uA, enhanced by 183%).

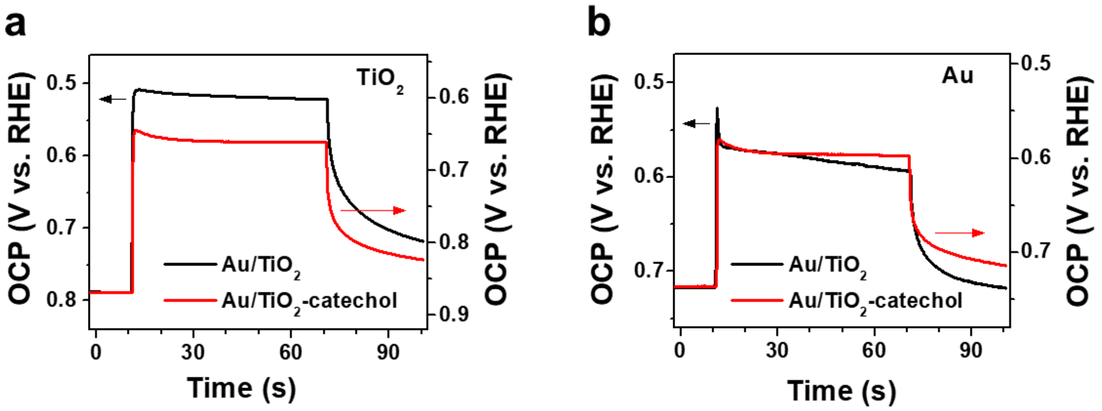

Figure S29. OCP curves obtained from (a) TiO_2 and (b) Au on a dual-working Au/TiO_2 electrode: pristine (black) and catechol-modified (red) Au/TiO_2 heterostructures. The light source was a 470 nm LED lamp (500 mW/cm^2). The light was turned on at 10 s and off at 70 s.

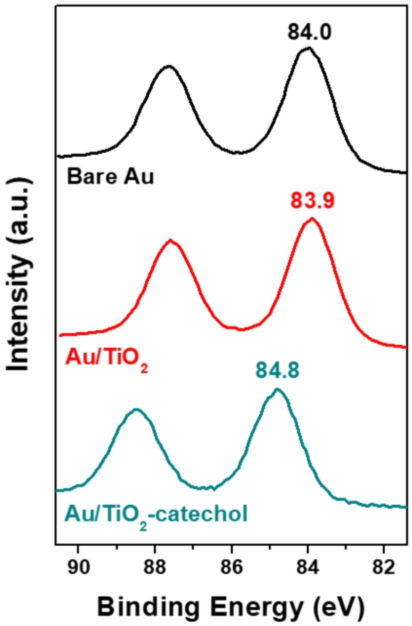

Figure S30. **Au 4f XPS spectra of a bare Au NP electrode, a pristine Au/TiO_2 electrode, and a catechol-modified Au/TiO_2 electrode.**

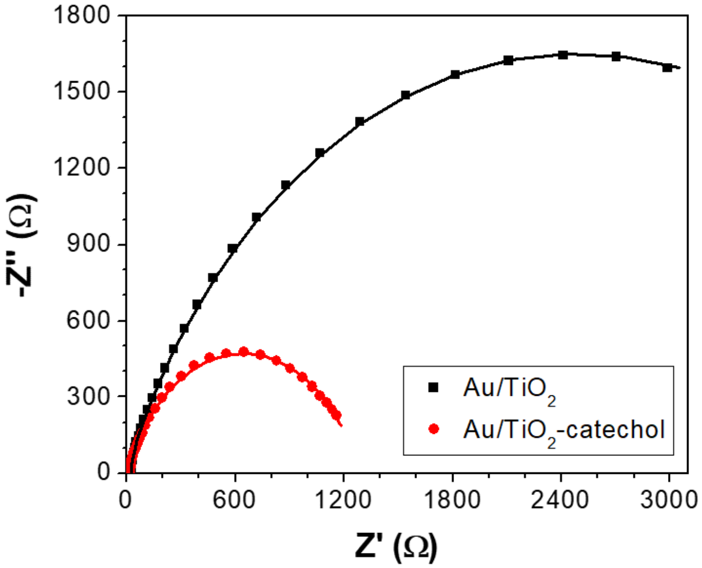

Figure S31. EIS on pristine (black) and catechol-modified (red) Au/TiO$_2$ electrodes at 0.8 V$_{RHE}$ under 470 nm illumination (500 mW/cm^2) in the unbuffered solution with pH 7.0. The capacitance of TiO$_2$-trapped holes (C_{trap}) decreased from 38.2 µF to 22.9 µF after the modification of catechol.

Supplementary Note 7. Catechol-modified TiO_2 electrodes

Previous studies reported that catechol adsorbed on TiO_2 also introduced visible-light activity owing to the LMCT (ligand to metal charge transfer) mechanism.[24-25] Figure S33 showed that modifying a TiO_2 electrode with catechol enhanced both photocurrent and V_{ph}. However, V_{ph} was found to decrease on the catechol-modified Au/TiO_2 electrode, excluding LMCT as the primary mechanism contributing to the enhanced photocurrent on the catechol-modified Au/TiO_2 electrode.

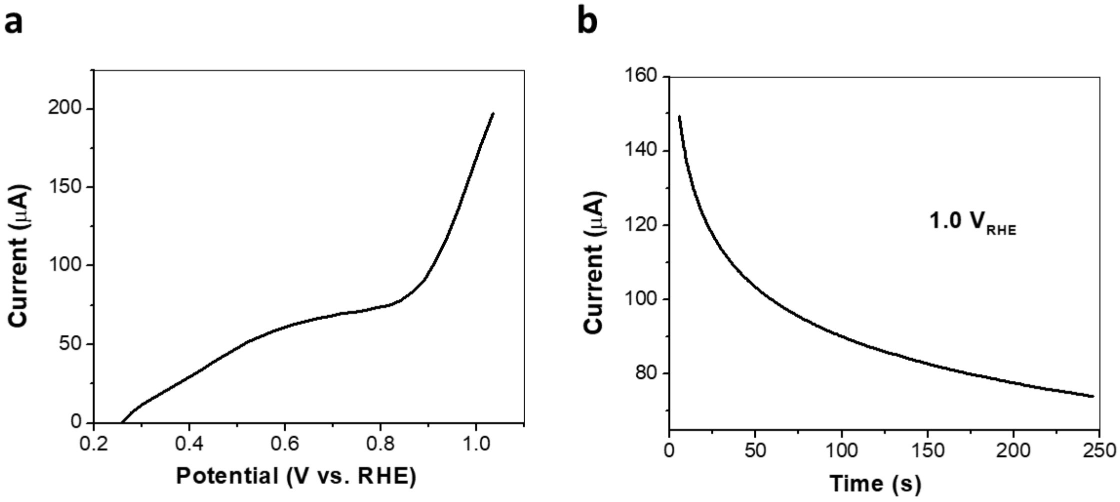

Figure S32. Photoelectrodeposition of catechol on a bare TiO_2 electrode. (**a**) LSV measurement of a TiO_2 electrode in the solution containing catechol (0.1 M). (**b**) Chronoamperometry performed at 1.0 V_{RHE} for 240 s. The light source was a 470 nm LED lamp (500 mW/cm^2).

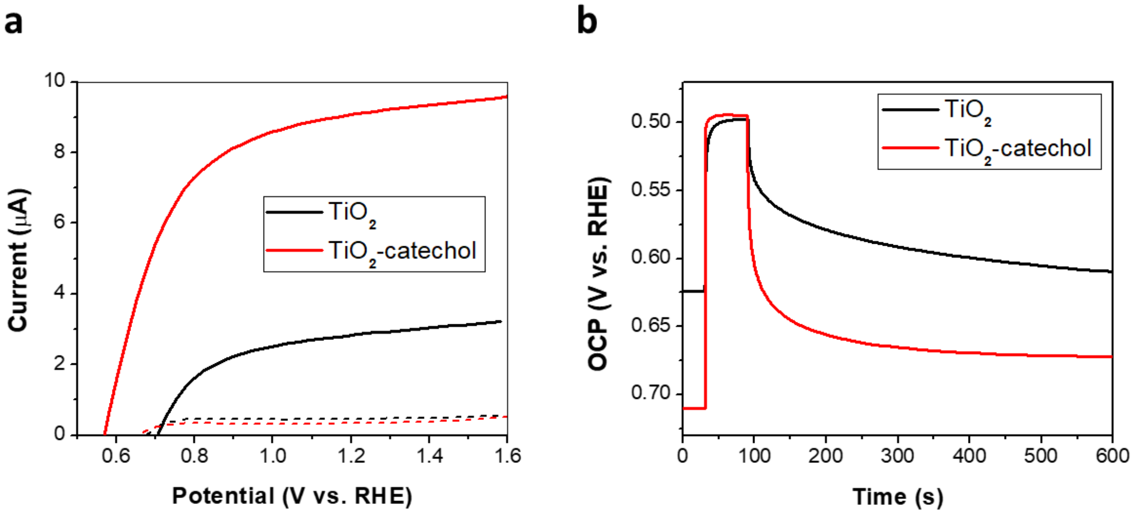

Figure S33. PEC behavior of the catechol-modified TiO_2 electrode. Data obtained from bare (black) and catechol-modified (red) TiO_2 electrodes. (**a**) LSV measurements under 470 nm illumination (solid lines) and in the dark (dashed lines). (**b**) OCP measurements under 470 nm illumination with the light turned on at 30 s and off at 90 s.

Supplementary Note 8. Rate law analysis on the catechol-modified Au/TiO_2 electrode

Analysis of the variation of reaction orders:

A = intermediate in RDS of water oxidation

B = holes trapped on TiO_2

C = holes trapped on catechol

D = holes on Au

(1) B + B → A

$$\frac{d[A]}{dt} = k_1[B][B] = k_1[B]^2$$

$$\ln\frac{d[A]}{dt} = \ln k_1 + 2\ln\,[B]$$

When RDS only involves two TiO_2-trapped holes, the reaction order of TiO_2-trapped holes is 2.

(2) B + C → A

$$\frac{d[A]}{dt} = k_1[B][C]$$

$$\ln\frac{d[A]}{dt} = \ln k_1 + \ln[B] + \ln\,[C]$$

When RDS involves one TiO_2-trapped hole and one catechol-trapped hole, the reaction order of TiO_2-trapped holes is 1.

(3) B + C → A; D + C → A

$$\frac{d[A]}{dt} = k_1[B][C] + k_2[D][C] = [C](k_1[B] + k_2[D])$$

$$\ln\frac{d[A]}{dt} = \ln[C] + \ln\,(k_1[B] + k_2[D])$$

When RDS involves two parallel elementary steps, the reaction order of TiO_2-trapped holes is below 1.

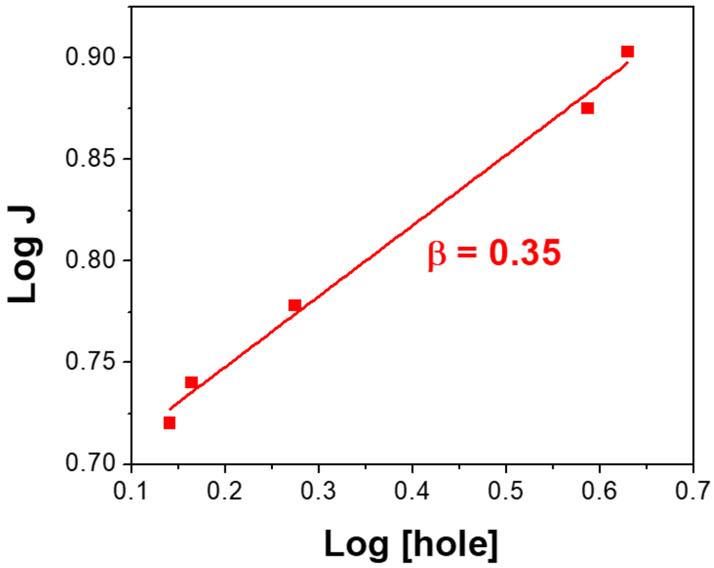

Figure S34. A reproduced result of the reaction order measurement on catechol-modified Au/TiO$_2$ electrodes. A new catechol-modified Au/TiO$_2$ electrode (different from the one used in the main text) was used and a similar reaction order was obtained.

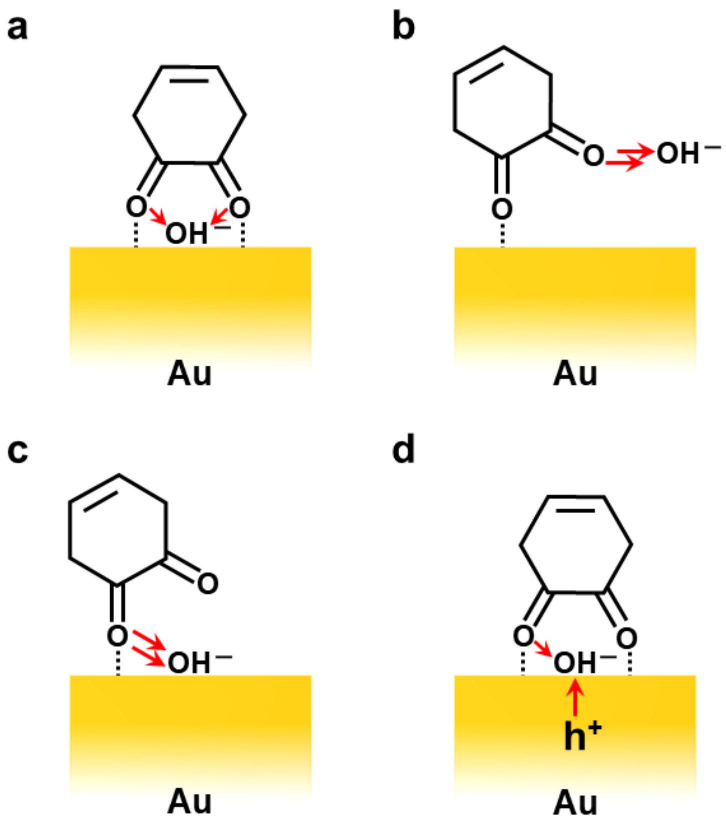

Figure S35. Multi-hole reaction pathways on catechol-modified Au surfaces. (**a**) The cooperation of two C=O unities provided two holes for driving water oxidation. (**b**) Water oxidation occurred via sequential oxidations of one hydroxyl group that was spatially away from Au surfaces. Two arrows indicated sequential hole transfers. (**c**) Water oxidation occurred via sequential oxidations of one hydroxyl group that adsorbed on Au surfaces. Two arrows indicated sequential hole transfers. (**d**) Cooperation between one hole initially trapped on catechol and one hole newly generated on Au.

Supplementary Note 9. Preparation of catechol-modified Au NP electrodes

Catechol was photoelectrodeposited on a Au NP electrode under 1.0 V_{RHE} and 470 nm irradiation for 600 s (Figure S36). After the deposition, the electrode was moved to a clean electrolyte (0.1 M $NaClO_4$ with pH 7.0) without catechol and fully charged by hot holes under 1.2 V_{RHE} and 470 nm irradiation for 1 h (Figure S37).

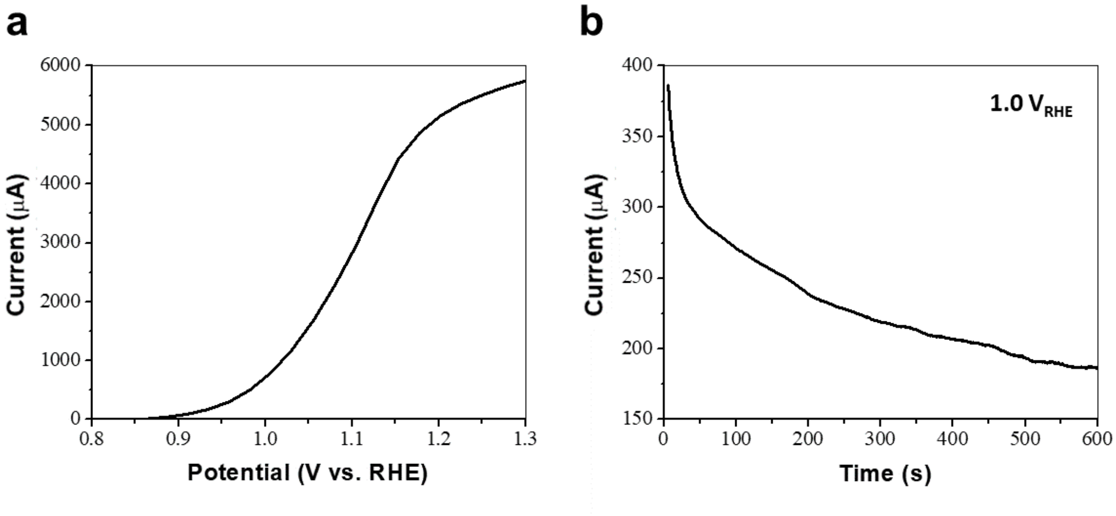

Figure S36. Photoelectrodeposition of catechol on a Au NP electrode. (**a**) LSV measurement of a Au NP electrode in the solution containing catechol (0.1 M). (**b**) Chronoamperometry performed at 1.0 V_{RHE} for 600 s. The light source was a 470 nm LED lamp (500 mW/cm^2).

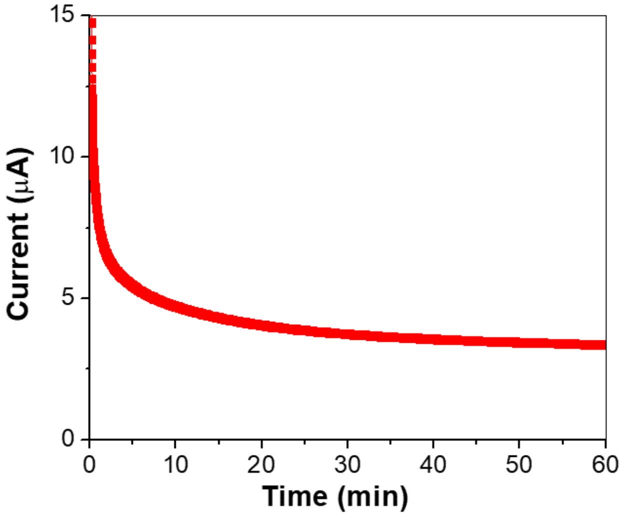

Figure S37. Charging of the catechol-modified Au NP electrode. A constant potential of 1.2 V_{RHE} was held on the Au/catechol electrode under 470 nm irradiation (500 mW/cm^2) for 1 h to fully charge the electrode with hot holes. The photocurrent reached a plateau, indicating that all hydroxyl groups were oxidized to ketone groups.

Supplementary Note 10. Comparisons among modified Au NP electrodes using catechol, 3,4-dihydroxybenzonitrile, and 4-nitrocatechol

Two catechol derivatives were used to modify Au NP electrodes, i.e., 3,4-dihydroxybenzonitrile (catechol with nitrile (-C≡N) substituent, abbreviated as cyanide-catechol), and 4-nitrocatechol. Cyanide-catechol was used for exploring the influence of adsorption mode (Figure 4d) on hot-hole stabilization and water oxidation. 4-nitrocatechol was used to study the influence of electronic effect on hot-hole stabilization due to the electron-withdrawing effect of its nitro group. LSV measurements showed that catechol and cyanide-catechol modified electrodes shared an identical onset potential (0.73 V_{RHE}, Figure 4a), indicating that oxidation potentials of hydroxyl groups on those adsorbates were the same. Therefore, the effect of adsorption mode was dominant when comparing PEC behaviors between catechol-modified and cyanide-catechol-modified Au NP electrodes as discussed in the main text. The 4-nitrocatechol-modified Au NP electrode exhibited an onset potential of ~ 0.76 V (Figure S39a), which was more anodic than that on the cyanide-catechol-modified electrode. This observation implied that it was more difficult to trap hot holes on 4-nitrocatechol molecules. However, the 4-nitrocatechol-modified Au NP electrode exhibited a higher photocurrent (0.31 μA, Figure S39b) than that of the cyanide-catechol-modified Au NP electrode (0.21 μA, Figure S39b) at 1.2 V_{RHE}. The higher photocurrent indicated that despite of its difficult hole trapping, 4-nitrocatechol-modified Au NP electrode still exhibited better performance in driving water oxidation. Noting that 4-nitrocatechol also adsorbed on Au NPs via hydroxyl groups (same as catechol). Hence, it was easier to drive water oxidation when hydroxyl groups adsorbed on Au surfaces even if the molecule was less prone to trap hot holes. It can be concluded that the effect of adsorption mode overwhelmed the electronic effect (i.e. ease of trapping holes on hydroxyl groups) in the Au/adsorbate system for water oxidation.

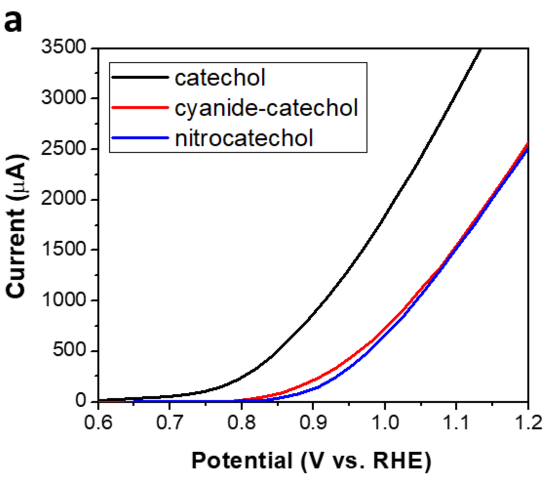

Figure S38. Fabrication of catechol derivatives-modified Au NP electrodes. (**a**) LSV measurements on Au NP electrodes in solutions containing catechol, cyanide-catechol, and 4-nitrocatechol, respectively. (**b**) Chronoamperometry performed at 1.0 V_{RHE} for 240 s. The light source was a 470 nm LED lamp (500 mW/cm^2).

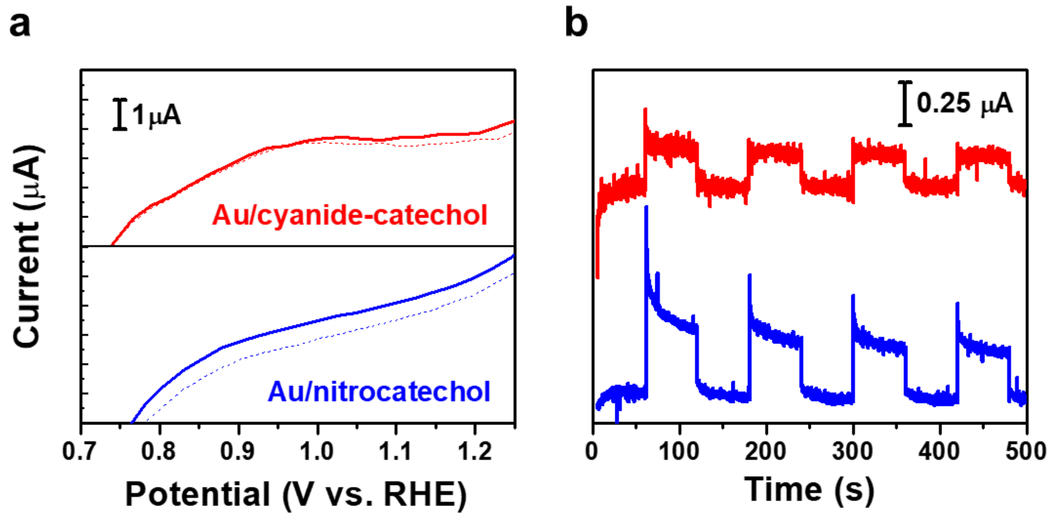

Figure S39. Comparison between 4-nitrocatechol-modified and cyanide-catechol-modified Au NP electrodes. (**a**) LSV traces and (**b**) chronoamperometry curves under 1.2 V_{RHE} with chopped light irradiation between Au/cyanide-catechol (red lines) and Au/4-nitrocatechol (blue lines) electrodes. The light source was a 470 nm LED lamp (500 mW/cm^2).

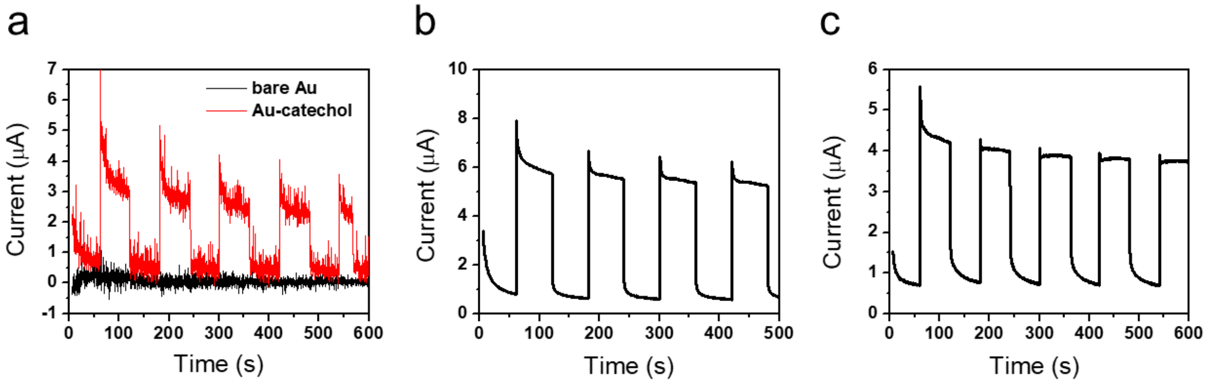

Figure S40. The reproducibility of catechol-mediated photocurrent enhancement on Au NP electrodes. The PEC water-oxidation activity of bare Au NP electrodes exhibited a highly reproducible value of ~ 0.2 uA. Hence, we only compare those catechol-modified electrodes in this case, without considering the minor difference among bare Au NP electrodes. This experiment was repeated for three times. Photocurrent results of 2.5 uA, 5.3 uA and 3.3 uA were obtained. The average value was 3.7 uA and the error was 1.2 uA.

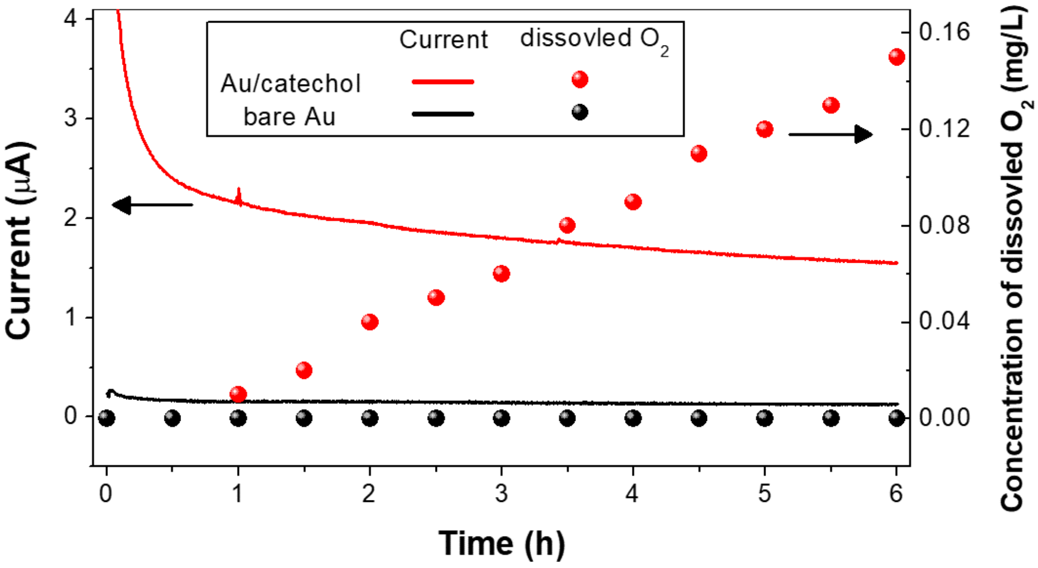

Figure S41. O_2 evolution test. A constant bias of 1.2 V_{RHE} was applied on bare and catechol-modified Au NP electrodes for 6 h. Solid lines showed the photocurrent during O_2 detection. Stable photocurrent of ~ 2 μA within 6 h was obtained on the Au/catechol electrode. The amount of produced O_2 was detected using a dissolved oxygen meter. Dots represented concentrations of dissolved O_2. The light source was a 470 nm LED lamp (500 mW/cm^2).

$$Q_{O_2} = 0.15 \times 20 \times 10^{-6}/32 \times 4 \times 96485 = 0.036\ \mathrm{C}$$

$$Q_{photocurrent} = 0.042\ \mathrm{C}$$

$$\mathrm{FE\%} = 86\%$$

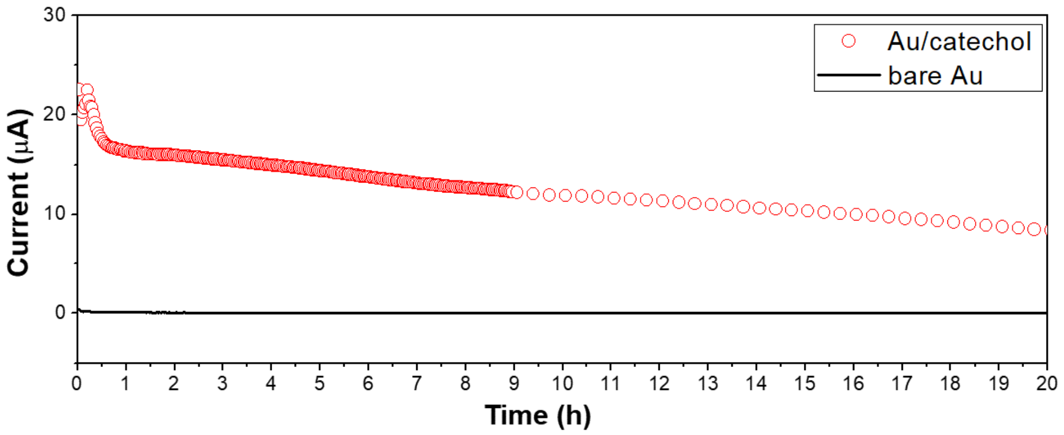

Figure S42 Long-term stability of a Au/catechol electrode. Photoelectrolysis performed on a Au/catechol electrode for 20 h at 1.2 V_{RHE}. The light source was a 470 nm LED lamp (500 mW/cm^2). Data was collected every 2 min before 9 hours and every 20 min afterward.

When further extending the reaction time, the photocurrent exhibited a very slow and continuous decayed within 20 hours. This decay should be due to the slow desorption of catechol molecules from Au surfaces under the harsh water-oxidation condition. Further improvement on the long-term stability of catechol-modified Au surfaces could be realized by molecular design, such as adding an Au-anchoring group adjacent to the hydroxyl group in catechol.

Supplementary Note 11. Catechol-modified FTO electrodes

The catechol-modified FTO electrode (**Figure S43**) showed a photocurrent of 0.20 μA (black curves, **Figure S44**), which was much lower than that on the Au/catechol electrode (3.28 μA, red curves, **Figure S44**). The oxidized catechol (i.e., quinone) was reported to be active for the photo-oxidation of water,[26] but one order of magnitude enhancement in the presence of Au NPs strongly suggested that Au surfaces provided much more active sites for driving water oxidation.

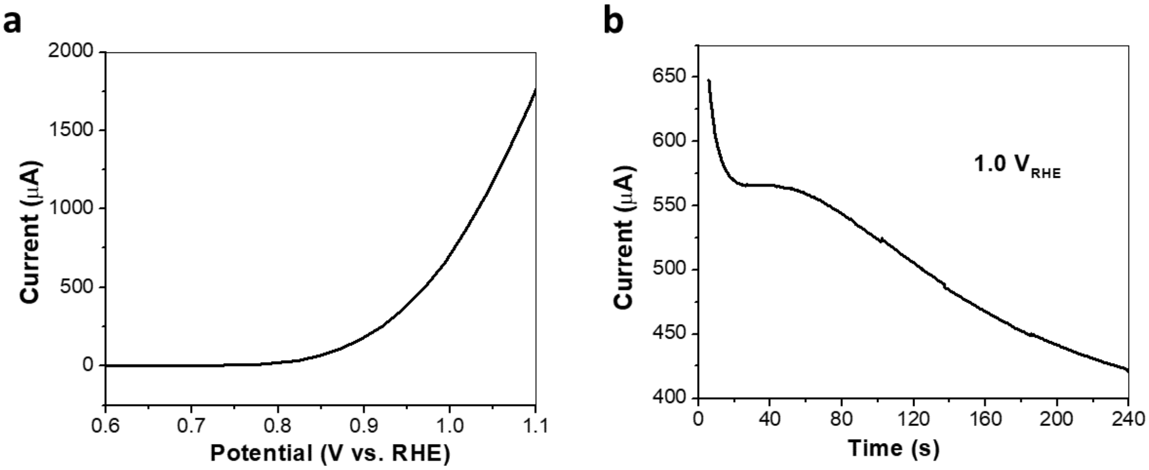

Figure S43. Photoelectrodeposition of catechol on an FTO electrode. (**a**) LSV measurement of an FTO electrode in the solution containing catechol (0.1 M). (**b**) Chronoamperometry performed at 1.0 V_{RHE} for 240 s. The light source was a 470 nm LED lamp (500 mW/cm^2).

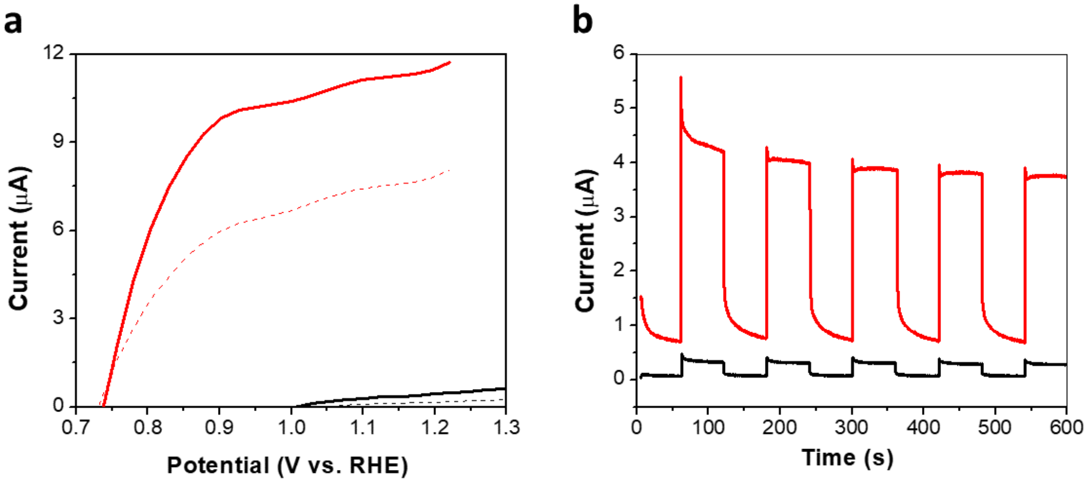

Figure S44. PEC behaviors of the catechol-modified FTO electrode and the catechol-modified Au electrode. Data obtained from the catechol-modified FTO electrode (black) and the catechol-modified Au NP electrode (red). (**a**) LSV measurements under 470 nm illumination (solid curves) and in the dark (dashed curves). (**b**) Chronoamperometry measurements under chopped 470 nm illumination at 1.2 V_{RHE}.

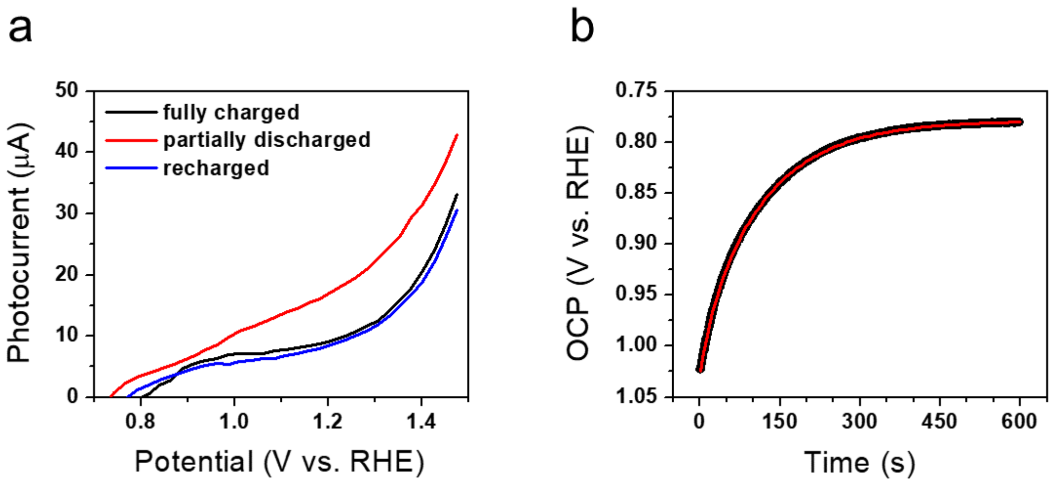

Figure S45. (a) Recovery of potential-photocurrent curves after turning bias off. (b) OCP measurement for detecting the recovery process. In figure a, the fully charged curve refers to that electrode was kept under the bias of 1.2 V_{RHE} for 6 h, in which all catechol molecules were converted to quinone. After turning of the bias for 600 s (the change of OCP was monitored as shown in figure b), part of quinone molecules released trapped holes and converted to hydroquinone, i.e., the partially discharged curve in figure a. After being recharged under the bias of 1.2 V_{RHE}, the I-V curve recovered to the first fully charged state (figure a).

References

1. DuChene, J. S.; Sweeny, B. C.; Johnston-Peck, A. C.; Su, D.; Stach, E. A.; Wei, W. D., Prolonged Hot Electron Dynamics in Plasmonic-Metal/Semiconductor Heterostructures with Implications for Solar Photocatalysis. Angew. Chem. Int. Ed. **2014,** *53*, 7887-7891.

2. Zhang, Y.; Zhang, H.; Ji, H.; Ma, W.; Chen, C.; Zhao, J., Pivotal Role and Regulation of Proton Transfer in Water Oxidation on Hematite Photoanodes. J. Am. Chem. Soc. **2016,** *138*, 2705-2711.

3. Sheng, H.; Li, Q.; Ma, W.; Ji, H.; Chen, C.; Zhao, J., Photocatalytic Degradation of Organic Pollutants on Surface Anionized TiO_2: Common Effect of Anions for High Hole-availability by Water. Appl. Catal. B: Environ **2013,** *138-139*, 212-218.

4. Sundararaman, R.; Narang, P.; Jermyn, A. S.; Goddard III, W. A.; Atwater, H. A., Theoretical Predictions for Hot-carrier Generation from Surface Plasmon Decay. Nat. Commun. **2014,** *5*, 5788.

5. Hung, S.-F.; Xiao, F.-X.; Hsu, Y.-Y.; Suen, N.-T.; Yang, H.-B.; Chen, H. M.; Liu, B., Iridium Oxide-Assisted Plasmon-Induced Hot Carriers: Improvement on Kinetics and Thermodynamics of Hot Carriers. Adv. Eng. Mater. **2016,** *6*, 1501339.

6. Schlather, A. E.; Manjavacas, A.; Lauchner, A.; Marangoni, V. S.; DeSantis, C. J.; Nordlander, P.; Halas, N. J., Hot Hole Photoelectrochemistry on Au@SiO_2@Au Nanoparticles. J. Phys. Chem. Lett. **2017,** *8*, 2060-2067.

7. Lin, F.; Boettcher, S. W., Adaptive Semiconductor/Electrocatalyst Junctions in Water-splitting Photoanodes. Nat. Mater. **2014,** *13*, 81-86.

8. Qiu, J.; Hajibabaei, H.; Nellist, M. R.; Laskowski, F. A. L.; Hamann, T. W.; Boettcher, S. W., Direct in Situ Measurement of Charge Transfer Processes During Photoelectrochemical Water Oxidation on Catalyzed Hematite. ACS Central Sci. **2017,** *3*, 1015-1025.

9. Aslam, U.; Chavez, S.; Linic, S., Controlling Energy Flow in Multimetallic Nanostructures for Plasmonic Catalysis. Nat. Nanotechnol. **2017,** *12*, 1000–1005.

10. Zhang, Y.; Jiang, S.; Song, W.; Zhou, P.; Ji, H.; Ma, W.; Hao, W.; Chen, C.; Zhao, J., Nonmetal P-doped Hematite Photoanode with Enhanced Electron Mobility and High Water Oxidation Activity. Energy Environ. Sci. **2015,** *8*, 1231-1236.

11. Zhang, Y.; Zhou, Z.; Chen, C.; Che, Y.; Ji, H.; Ma, W.; Zhang, J.; Song, D.; Zhao, J., Gradient $FeO_x(PO_4)_y$ Layer on Hematite Photoanodes: Novel Structure for Efficient Light-Driven Water Oxidation. ACS Appl. Mater. Interfaces **2014,** *6*, 12844-12851.

12. Klahr, B.; Gimenez, S.; Fabregat-Santiago, F.; Bisquert, J.; Hamann, T. W., Electrochemical and Photoelectrochemical Investigation of Water Oxidation with Hematite Electrodes. Energy Environ. Sci. **2012,** *5*, 7626-7636.

13. Klahr, B.; Gimenez, S.; Fabregat-Santiago, F.; Hamann, T.; Bisquert, J., Water Oxidation at Hematite Photoelectrodes: the Role of Surface States. J. Am. Chem. Soc. **2012,** *134*, 4294-302.

14. Le Formal, F.; Pastor, E.; Tilley, S. D.; Mesa, C. A.; Pendlebury, S. R.; Grätzel, M.; Durrant, J. R., Rate Law Analysis of Water Oxidation on a Hematite Surface. J. Am. Chem. Soc. **2015,** *137*, 6629-6637.

15. Zhang, Y.; Zhang, H.; Liu, A.; Chen, C.; Song, W.; Zhao, J., Rate-Limiting O–O Bond Formation Pathways for Water Oxidation on Hematite Photoanode. J. Am. Chem. Soc. **2018,** *140*, 3264-3269.

16. Nakamura, R.; Nakato, Y., Primary Intermediates of Oxygen Photoevolution Reaction on TiO_2 (Rutile) Particles, Revealed by in Situ FTIR Absorption and Photoluminescence Measurements. J. Am. Chem. Soc. **2004,** *126*, 1290-1298.

17. Migani, A.; Blancafort, L., What Controls Photocatalytic Water Oxidation on Rutile TiO_2(110) under Ultra-High-Vacuum Conditions? J. Am. Chem. Soc. **2017,** *139*, 11845-11856.

18. Liu, F.; Feng, N.; Wang, Q.; Xu, J.; Qi, G.; Wang, C.; Deng, F., Transfer Channel of Photoinduced Holes on a TiO_2 Surface As Revealed by Solid-State Nuclear Magnetic Resonance and Electron Spin Resonance Spectroscopy. J. Am. Chem. Soc. **2017,** *139*, 10020-10028.

19. Shirai, K.; Fazio, G.; Sugimoto, T.; Selli, D.; Ferraro, L.; Watanabe, K.; Haruta, M.; Ohtani, B.; Kurata, H.; Di Valentin, C.; Matsumoto, Y., Water-Assisted Hole Trapping at the Highly Curved Surface of Nano-TiO_2 Photocatalyst. J. Am. Chem. Soc. **2018,** 4, 1415-1422.

20. Cheng, J.; Sprik, M., Acidity of the Aqueous Rutile TiO_2(110) Surface from Density Functional Theory Based Molecular Dynamics. J. Chem Theo. and Comput. **2010,** *6*, 880-889.

21. Zheng, B. Y.; Zhao, H.; Manjavacas, A.; McClain, M.; Nordlander, P.; Halas, N. J., Distinguishing Between Plasmon-induced and Photoexcited Carriers in a Device Geometry. Nat. Commun. **2015,** *6*, 7797.

22. Christopher, P.; Moskovits, M., Hot Charge Carrier Transmission from Plasmonic Nanostructures. Annu. Rev. Phys. Chem. **2017,** *68*, 379-398.

23. Wu, K.; Chen, J.; McBride, J. R.; Lian, T., Efficient Hot-electron Transfer by a Plasmon-induced Interfacial Charge-transfer Transition. Science **2015,** *349*, 632-635.

24. Lana-Villarreal, T.; Rodes, A.; Pérez, J. M.; Gómez, R., A Spectroscopic and Electrochemical Approach to the Study of the Interactions and Photoinduced Electron Transfer between Catechol and Anatase Nanoparticles in Aqueous Solution. J. Am. Chem. Soc. **2005,** *127*, 12601-12611.

25. Tachan, Z.; Hod, I.; Zaban, A., The TiO_2–Catechol Complex: Coupling Type II Sensitization with Efficient Catalysis of Water Oxidation. Adv. Eng. Mater. **2014,** *4*, 1301249.

26. Pochon, A.; Vaughan, P. P.; Gan, D.; Vath, P.; Blough, N. V.; Falvey, D. E., Photochemical Oxidation of Water by 2-Methyl-1,4-benzoquinone: Evidence against the Formation of Free Hydroxyl Radical. J. Phys. Chem. A **2002,** *106*, 2889-2894.